

# X-ray four-wave mixing in molecules

Satoshi Tanaka

*Department of Chemistry, University of Rochester, Rochester, New York 14627  
and College of Integrated Arts and Sciences, Osaka Prefecture University, Sakai 599-8531, Japan*

Shaul Mukamel

*Department of Chemistry, University of Rochester, Rochester, New York 14627*

(Received 30 August 2001; accepted 2 November 2001)

An effective core-exciton Hamiltonian is constructed for nitroanilines which includes  $1s$  core hole transitions of both nitrogen atoms. The wavevector and frequency dependent third order susceptibility  $\chi^{(3)}$  is calculated and used to predict the frequency-domain pump-probe spectra which show both photobleaching and excited state absorption components. Signatures of electron delocalization and differences among the para-, meta-, and ortho-isomers are discussed. © 2002 American Institute of Physics. [DOI: 10.1063/1.1429950]

## I. INTRODUCTION

Recent advances in synchrotron radiation intense light sources have opened up a new era in soft x-ray spectroscopy. The dramatic improvements of spectral resolution in x-ray absorption<sup>1,2</sup> and x-ray photoemission spectra<sup>3</sup> have revealed a fine structure which provides the most valuable information on electronic states and vibrational couplings in core excited states.

Third generation synchrotron radiation sources, which are extremely bright in the vacuum ultraviolet, soft x-ray, and hard x-ray regions, also make it possible to obtain resonant x-ray emission and resonant Auger emission spectra in solid crystals, thin films, gaseous molecules, and adsorbates on surfaces.<sup>4–6</sup> Both are coherent second order quantum processes described by the Heisenberg–Kramers formula, and the signal intensities depend on both of the incoming x-ray energy and the emitted x-ray (Auger electron kinetic) energy. The correlations between the incoming and the emission energies in these spectra provide more information on the electronic states and the relaxation dynamics of the core excited states in various systems than linear techniques, such as x-ray absorption and photoemission.

As the intensity of the x-ray beam increases, the nonlinear response of the material to the x-ray field may be observed. The lowest order x-ray nonlinear spectroscopies are sum and difference frequency generation (second-order). Four-wave mixing (third-order) techniques include third-harmonic generation, pump-probe, hole burning, photon-echo, transient grating, and coherent Raman scattering (CRS). Conceptually resonant x-ray and Auger emission spectroscopies are also related to third-order nonlinear spectroscopies,<sup>7–9</sup> even though technically they are linear, i.e., the signal intensities of resonant x-ray and Auger emission processes are proportional to the incoming x-ray intensity, where the x-ray photon or Auger electron is spontaneously emitted by the material.

Rapid progress has also taken place in the development of intense femtosecond short x-ray pulses. X-ray pulses as short as 300 fs have been reported.<sup>10</sup> Numerous experiments

have been reported on time-resolved x-ray diffraction<sup>11–14</sup> and time-resolved x-ray absorption,<sup>15,16</sup> where the material is first excited by an optical pump pulse followed by the x-ray probe. However, intense x-ray pulses are typically still long compared with a core hole lifetime ( $\leq 10$  fs) determined by nonradiative Auger decay, so that time-resolved nonlinear spectroscopy experiments require x-ray pulses shorter than the core hole lifetime. 650 attosecond soft x-ray pulses have been produced by high harmonic generation but the intensities are still too weak for carrying out nonlinear spectroscopy.<sup>17</sup>

In our previous papers,<sup>7,8</sup> we have developed a unified correlation-function theory for x-ray nonlinear spectroscopies based on nonlinear response functions (NRF's), which are given by combinations of multitime correlation functions of the current density operator. Their frequency domain analogs are the nonlinear susceptibilities  $\chi^{(n)}$  used to describe stationary experiments. NRF's are expressed as sums of *Liouville-space pathways*, which provide an intuitive picture for the time evolution of the density matrix.

In this paper we apply this formulation to calculate the stationary x-ray four-wave mixing signals of para-nitroaniline (pNA), meta-nitroaniline (mNA), and ortho-nitroaniline (oNA) (Fig. 1). Nitroanilines are typical push-pull, donor-acceptor molecules, and the mechanism of intramolecular charge transfer upon the core excitation has been extensively studied by x-ray photoemission and absorption spectroscopies.<sup>18–22</sup> Intramolecular charge transfer strongly depends on the spatial coherence of the excited states.

Core excited states are usually strongly localized around the excited atom due to the attractive core hole potential for the excited electron. This suggests that the x-ray absorption spectrum may be calculated using the *building block picture*, i.e., the spectrum is simply given by the sum of the absorption spectrum for blocks of atoms or group of atoms in a molecule.<sup>23,24</sup> The success of this approach depends heavily on the degree of coherence of core excited states. We examine the information contained in four-wave mixing spectra and demonstrate that x-ray pump-probe spectroscopy should

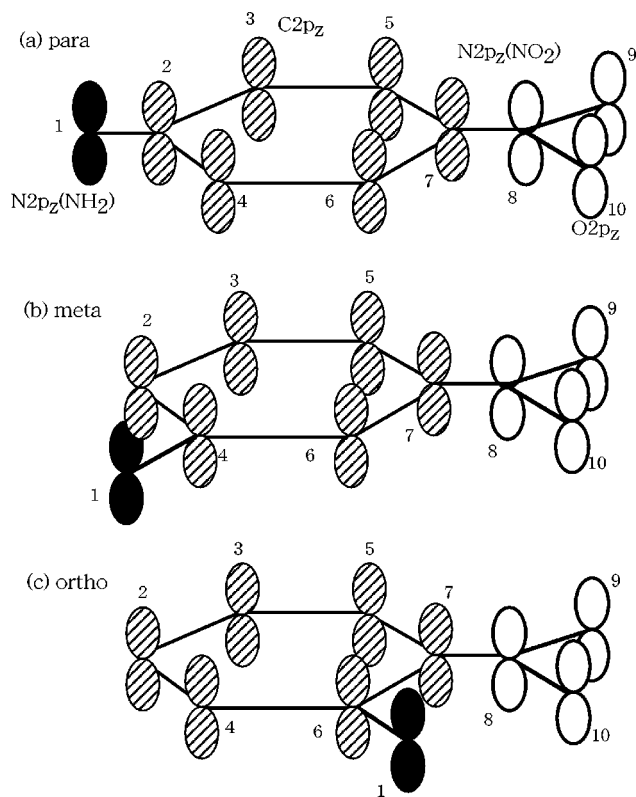


FIG. 1. Molecular structure of (a) para-, (b) meta-, and (c) ortho-nitroaniline.

be a powerful tool for investigating the spatial coherence of the excited states. There are many x-ray four-wave mixing techniques which, like pump-probe, depend on the third order susceptibility  $\chi^{(3)}$ . These include transient gratings, coherent Raman, sum and difference frequency generation. These may also be calculated using the present approach and could give new insights into excited state coherence.

The core exciton model is presented in Sec. II. Formal expressions of  $\chi^{(3)}$  are given in the appendices. Numerical calculations of x-ray linear absorption of nitroanilines are presented in Sec. III and the pump-probe spectra for the various isomers are discussed in Sec. IV. Concluding remarks are given in Sec. V.

## II. THE CORE EXCITON HAMILTONIAN

Since the low lying valence states of nitroanilines mainly consist of  $\pi$  orbitals, we consider the atomic orbital (AO) basis set shown in Fig. 1, which includes the  $2p_z$  atomic orbitals at each site. Using this basis set we construct the following tight binding Hamiltonian for the  $\pi$  system,

$$\hat{H}_{MO} = \sum_m \epsilon_m c_{m\sigma}^\dagger c_{m\sigma} + \sum_{m,n} \sum_{\sigma} t_{mn} c_{m\sigma}^\dagger c_{n\sigma}, \quad (1)$$

where  $\epsilon_m$  denotes the energy of the  $2p_z$  AOs at the  $m$ th site and  $t_{nm}$  are the transfer integrals.

To obtain these parameters we first performed a MNDO-SCF electronic structure calculation and computed the MO level structure. These parameters are then determined by fitting the eigenvalues of  $\hat{H}_{MO}$  with that calculation.<sup>25</sup> The re-

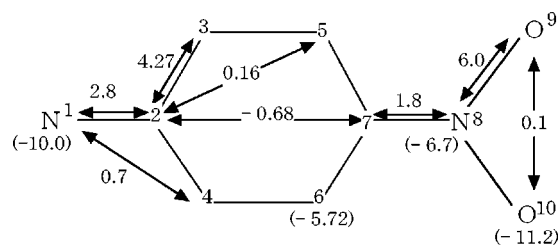


FIG. 2. Parameters of  $\hat{H}_{MO}$  of pNA determined by fitting the eigenvalues of  $\hat{H}_{MO}$  with MNDO-SCF calculation. The values in parentheses are the energies of the AOs.

sulting parameters for pNA are shown in Fig. 2 and the molecular orbital (MO) energies are displayed in Fig. 3(c). For mNA and oNA, we used the same parameters, assuming the same transfer integrals between the N  $2p_z$  at site 1 and the nearest (2.8 eV) and second nearest neighbor C atoms (0.7 eV) in the benzene ring.

To identify the character of each MO, we show the AO levels in Figs. 3(a) and 3(e): The C  $2p_z$  AOs on the benzene ring, the N  $2p_z$  AO at the 1st site, and the N  $2p_z$  and O  $2p_z$  AOs located at the NO<sub>2</sub> group in Fig. 1. The C  $2p_z$  AOs are split into bonding and antibonding orbitals as shown in (b). Since the N  $2p_z$  AO level is far below the antibonding C  $2p_z$  MOs, the N  $2p_z$ (NH<sub>2</sub>) AO component is only slightly mixed with the unoccupied antibonding MOs, but is strongly mixed with the C  $2p_z$  bonding MOs. The N  $2p_z$ (NO<sub>2</sub>) AO and the O  $2p_z$  AOs are strongly coupled causing its antibonding state  $\pi^*(\text{NO}_2)$  to be close to the  $\pi^*(\text{C}=\text{C}+\text{NH}_2)$  MOs. [see Fig. 3(d)] Thus the  $\pi^*(\text{NO})$  state is strongly coupled to the  $\pi^*(\text{C}=\text{C}+\text{NH}_2)$  MOs, so that there is a considerable

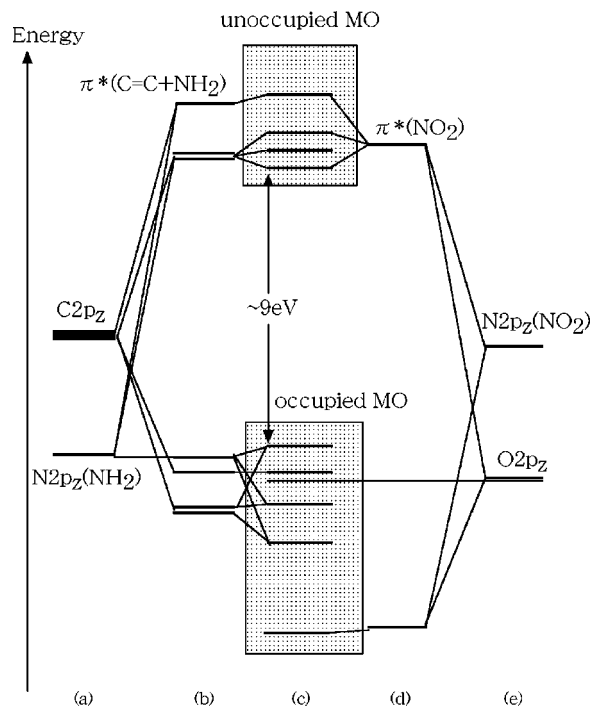


FIG. 3. Energy level scheme showing the atomic orbitals (AOs) and the molecular orbitals (MOs).

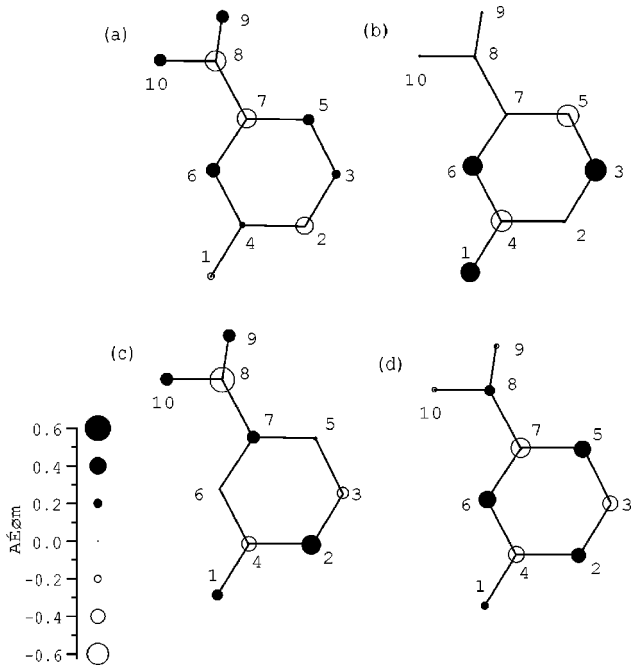


FIG. 4. The coefficients  $A_{\alpha m}$  [Eq. (2)] for the unoccupied antibonding MOs of mNA: (a) to (d) in order of increasing energy. The N(1)  $2p_z$  AO component  $A_{\alpha 1}$  are multiplied  $\times 4$ .

amount of the N  $2p_z$ (NO<sub>2</sub>) AO component in the unoccupied antibonding MOs. [Fig. 3(c)].

The MOs  $|\alpha\rangle$  with energy  $\epsilon_\alpha$  are given by

$$|\alpha\rangle = \sum_{m=1}^{10} A_{\alpha m} |m\rangle, \quad (2)$$

where  $|m\rangle$  stands for the  $2p_z$  orbital at the  $m$ th site, and the coefficients  $A_{\alpha m}$  are obtained by diagonalizing  $\hat{H}_{MO}$ . We denote the electron creation operator for the  $\alpha$  MO with spin  $\sigma$  by  $c_{\alpha\sigma}^\dagger$ . The coefficients  $A_{\alpha m}$  of mNA for the unoccupied antibonding MOs are displayed in Fig. 4.

In the following calculations we assume that both pump and probe x-ray energies are scanned across the N  $1s$  core-excitation energies to the antibonding MOs. Since these molecules have two nonequivalent N atoms, we need consider two N  $1s$  core orbitals located at the site 1 and 8. We denote the creation operator for the core electron at the  $l$ th site with spin  $\sigma$  by  $a_{l\sigma}^\dagger$  ( $l=1,8$ ), where 1 and 8 represent the states where a N  $1s$  core hole is localized at site 1 in Fig. 1 (NH<sub>2</sub>) and site 8 (NO<sub>2</sub>), respectively. The LUMO-HOMO gap (9 eV) is large, allowing us to focus solely on the four unoccupied antibonding MOs for  $\alpha$ : Altogether our model has thus six relevant orbitals (2 core + 4 valence).

We next construct the effective space of active global electronic states. Denoting the ground state of the  $\pi$  system by  $|\text{vac}\rangle$ , the molecular ground state  $|g\rangle$  is

$$|g\rangle = a_{1\uparrow}^\dagger a_{1\downarrow}^\dagger a_{8\uparrow}^\dagger a_{8\downarrow}^\dagger |\text{vac}\rangle. \quad (3)$$

The model has 8 single-core global excited states

$$|1, \underline{1}; \alpha\rangle = \frac{1}{2}(a_{1\uparrow} c_{\alpha\uparrow}^\dagger + a_{1\downarrow} c_{\alpha\downarrow}^\dagger) |g\rangle, \quad (4a)$$

$$|8, \underline{8}; \alpha\rangle = \frac{1}{2}(a_{8\uparrow} c_{\alpha\uparrow}^\dagger + a_{8\downarrow} c_{\alpha\downarrow}^\dagger) |g\rangle, \quad (4b)$$

with  $\alpha=1, \dots, 4$  runs over the antibonding MO.

To describe the x-ray four-wave mixing process we also need to take into account the double-core-excited states reached by an excitation from the single core excited state with an x-ray probe beam. Depending on their spin and orbital configurations, the double-core-excited states are classified into the following four subspaces:

$$|1, \underline{1}; \alpha, \beta\rangle = -\frac{1}{\sqrt{2}} a_{1\uparrow} a_{1\downarrow} (c_{\alpha\uparrow}^\dagger c_{\beta\downarrow}^\dagger - c_{\alpha\downarrow}^\dagger c_{\beta\uparrow}^\dagger) |g\rangle (\alpha < \beta) \quad (5a)$$

$$|8, \underline{8}; \alpha, \beta\rangle = -\frac{1}{\sqrt{2}} a_{8\uparrow} a_{8\downarrow} (c_{\alpha\uparrow}^\dagger c_{\beta\downarrow}^\dagger - c_{\alpha\downarrow}^\dagger c_{\beta\uparrow}^\dagger) |g\rangle (\alpha < \beta) \quad (5b)$$

$$|1, \underline{8}; \alpha, \beta(\text{para})\rangle = \frac{1}{\sqrt{2}} (a_{8\uparrow} c_{\alpha\uparrow}^\dagger a_{1\uparrow} c_{\beta\uparrow}^\dagger + a_{8\downarrow} c_{\alpha\downarrow}^\dagger a_{1\downarrow} c_{\beta\downarrow}^\dagger) |g\rangle (\alpha < \beta) \quad (5c)$$

$$|1, \underline{8}; \alpha, \beta(\text{antipara})\rangle = \frac{1}{\sqrt{2}} (a_{8\uparrow} c_{\alpha\uparrow}^\dagger a_{1\downarrow} c_{\beta\downarrow}^\dagger + a_{8\downarrow} c_{\alpha\downarrow}^\dagger a_{1\uparrow} c_{\beta\uparrow}^\dagger) |g\rangle. \quad (5d)$$

For  $\alpha = \beta$ , we have

$$|1, \underline{1}; \alpha, \alpha\rangle = -a_{1\uparrow} a_{1\downarrow} c_{\alpha\uparrow}^\dagger c_{\alpha\downarrow}^\dagger |g\rangle, \quad (6a)$$

$$|8, \underline{8}; \alpha, \alpha\rangle = -a_{8\uparrow} a_{8\downarrow} c_{\alpha\uparrow}^\dagger c_{\alpha\downarrow}^\dagger |g\rangle. \quad (6b)$$

Altogether there are 42 double-core-excited states.

Using our 51 state active space we finally construct the total model Hamiltonian,

$$\hat{H}_{\text{tot}} = \hat{H}_v + \hat{H}_c + \hat{U}_{cv}, \quad (7a)$$

$$\hat{H}_v = \sum_{\alpha} \sum_{\sigma} \epsilon_{\alpha} c_{\alpha\sigma}^\dagger c_{\alpha\sigma} + \frac{1}{2} \sum_{\alpha_1 \alpha_2 \alpha_3 \alpha_4} \sum_{\sigma \sigma'} u_v(\alpha_1 \alpha_2; \alpha_3 \alpha_4) \times c_{\alpha_1 \sigma}^\dagger c_{\alpha_2 \sigma'}^\dagger c_{\alpha_3 \sigma'} c_{\alpha_4 \sigma}, \quad (7b)$$

$$\hat{H}_c = \sum_{l=1,8} \epsilon_l a_{l\sigma}^\dagger a_{l\sigma} + \frac{1}{2} \sum_{l,m=1,8} \sum_{\sigma \sigma'} u_c(l; m) a_{l\sigma}^\dagger a_{m\sigma'}^\dagger a_{m\sigma'} a_{l\sigma}, \quad (7c)$$

$$\hat{U}_{cv} = - \sum_{l=1,8} \sum_{\alpha_1 \alpha_2} \sum_{\sigma \sigma'} u_{lv}(\alpha_1; \alpha_2) (1 - a_{l\sigma}^\dagger a_{l\sigma}) c_{\alpha_1 \sigma'}^\dagger c_{\alpha_2 \sigma'}. \quad (7d)$$

The first terms in  $\hat{H}_v$  and  $\hat{H}_c$  represent the energies of the MOs ( $\epsilon_\alpha$ ) and the core states ( $\epsilon_l$ ), respectively, and the second terms represent the Coulomb repulsion between the valence electrons and between the core holes, respectively.  $\hat{U}_{cv}$  is the attractive Coulomb potential between the core hole and the excited electron.

In Eq. (7) we assume on-site Coulomb interactions (Hubbard model, see Appendix D). The on-site Coulomb in-

TABLE I. Parameter values used in the calculation (in eV).

$u_v$	$\epsilon_{\underline{1}}$	$\epsilon_{\underline{8}}$	$u_{\underline{1}}$	$u_{\underline{8}}$	$\frac{u_c}{(1;1)}$	$\frac{u_c}{(8;8)}$	$\frac{u_c}{(1;8)}$	$\gamma_g^a$	$\gamma_e^b$	$\gamma_f^c$
3.4	402.9	407.9	8.0	6.0	15.0	15.0	3.0	0.01	0.092	0.184

<sup>a</sup>This value of  $\gamma_g$  is used for avoiding a fictitious divergence in  $I_{gg}(\omega)$ .

<sup>b</sup>Taken from Ref. 35.

<sup>c</sup> $\gamma_f = 2\gamma_e$ .

interactions  $u_v$  and  $u_l$  and the Coulomb repulsion for the core holes  $u_c(l; m)$  parameters in Eqs. (7a) and (7c) are then given by

$$u_v(\alpha_1\alpha_2; \alpha_3\alpha_4) = u_v \sum_{i=1}^{10} A_{\alpha_1, i}^* A_{\alpha_2, i}^* A_{\alpha_3, i} A_{\alpha_4, i}, \quad (8a)$$

$$u_{lv}(\alpha_1; \alpha_2) = u_l A_{\alpha_1, l}^* A_{\alpha_2, l}. \quad (8b)$$

These parameters are listed in Table I.

The active energy level scheme is schematically depicted in Fig. 5. The energy levels for the single N 1s (NO<sub>2</sub>) core excited state lie above the N 1s (NH<sub>2</sub>) single core excited state, because of the difference of the ionization potential of the N 1s orbitals. (See Table I). In addition, the level spacings are also different, because of the difference of the core potential effect mentioned earlier.

Since the repulsive Coulomb potential is much stronger when the two core holes are located on the same site ( $|l, l; \alpha, \beta\rangle$ ,  $l = \underline{1}$  or  $\underline{8}$ ) than on different sites ( $|\underline{1}, \underline{8}; \alpha, \beta\rangle$ ), we expect the energy levels for the former states to be higher.

The coupling of the molecule with a resonant radiation field is <sup>7</sup>

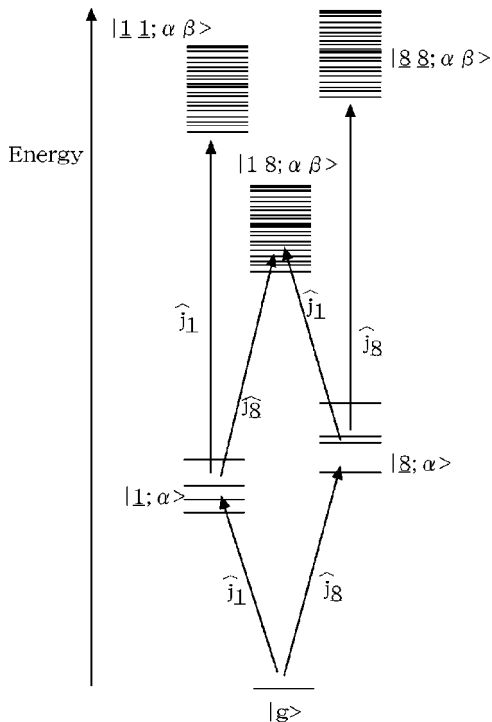


FIG. 5. Level scheme of the many electron states for the ground, single-core-excited states, and double-core-excited states of nitroaniline.

$$\hat{H}_{\text{int}} = - \int d\mathbf{r} \hat{\mathbf{j}}(\mathbf{r}) \cdot \hat{\mathbf{A}}(\mathbf{r}, t) d\mathbf{r}, \quad (9)$$

where  $\hat{\mathbf{A}}(\mathbf{r}, t)$  is a vector potential of the radiation field.  $\hat{\mathbf{j}}(\mathbf{r})$  is the atomic current-density operator defined by

$$\hat{\mathbf{j}}(\mathbf{r}) = \sum_{l=\underline{1}, \underline{8}} \delta(\mathbf{r} - \mathbf{R}_l) \hat{\mathbf{j}}_l, \quad (10)$$

where  $\mathbf{R}_l$  denotes the  $l$ th atomic position,

$$\hat{\mathbf{j}}_l = \sum_{\alpha\sigma} (j_{l,\alpha} a_{l\sigma} c_{\alpha\sigma}^\dagger + H.c.) \quad (l = \underline{1}, \underline{8}), \quad (11)$$

and the coefficients  $j_{l,\alpha}$  are

$$j_{l,\alpha} \equiv \frac{e\hbar}{mi} \int d^3\mathbf{r} \psi_\alpha^*(\mathbf{r}) \nabla \phi_l(\mathbf{r}) \quad (12a)$$

$$= \mu_l A_{\alpha, l}^*. \quad (12b)$$

In Eq. (12),  $\mu_l$  is the strength of the atomic current density operator for the transition of the N 1s core electron at the  $l$ th site. The ratio of  $\mu_{\underline{1}}$  and  $\mu_{\underline{8}}$  given in Table I was adjusted to reproduce the experimental x-ray absorption spectra. We only retain on-site atomic transitions and neglect the cross transitions between orbitals at different atomic sites.

### III. X-RAY ABSORPTION IN THE NITROGEN 1 s REGION

The eigenstates of  $\hat{H}_{\text{tot}}$  are obtained by diagonalizing the  $51 \times 51$   $\hat{H}_{\text{tot}}$  matrix represented in the basis set of Eqs. (3), (4), (5), and (6). The absorption spectra were calculated using the transition matrix element of the current density (11). The calculated N 1s x-ray absorption spectra for pNA, mNA, and oNA are shown in Fig. 6, where the N 1s core excitations from N (NH<sub>2</sub>) atom and N (NO<sub>2</sub>) atom are given by the black and the gray line spectra, respectively. Hereafter we denote the N atoms of NH<sub>2</sub> and NO<sub>2</sub> as N(1) and N(8), respectively. We shall first focus on mNA. The absorption spectrum consists of 8 lines: 4 black [excitations from N (NH<sub>2</sub>) atom] and 4 gray [excitations from N (NO<sub>2</sub>) atom]. The peak positions and the intensity distribution of the black and gray lines are different due to difference of the core exciton effects.

To analyze these effects, we have calculated two density matrices. The first is the single electron density matrix of the  $\alpha$  orbital,

$$\rho_{g;nm}^\alpha \equiv \sum_{\sigma\sigma'} \langle \alpha | c_{m\sigma}^\dagger c_{n\sigma'} | \alpha \rangle. \quad (13)$$

$\rho_{g;nm}^\alpha$  are shown in the left column of Fig. 7 for antibonding MOs. The axes are labeled by the site number shown in Fig. 1. We next consider the density matrix for the single-core exciton state,

$$\rho_{l;nm}^\xi \equiv \sum_{\sigma\sigma'} \langle \Psi_\xi | c_{m\sigma'}^\dagger c_{n\sigma} a_{l\sigma}^\dagger a_{l\sigma} | \Psi_\xi \rangle, \quad (14)$$

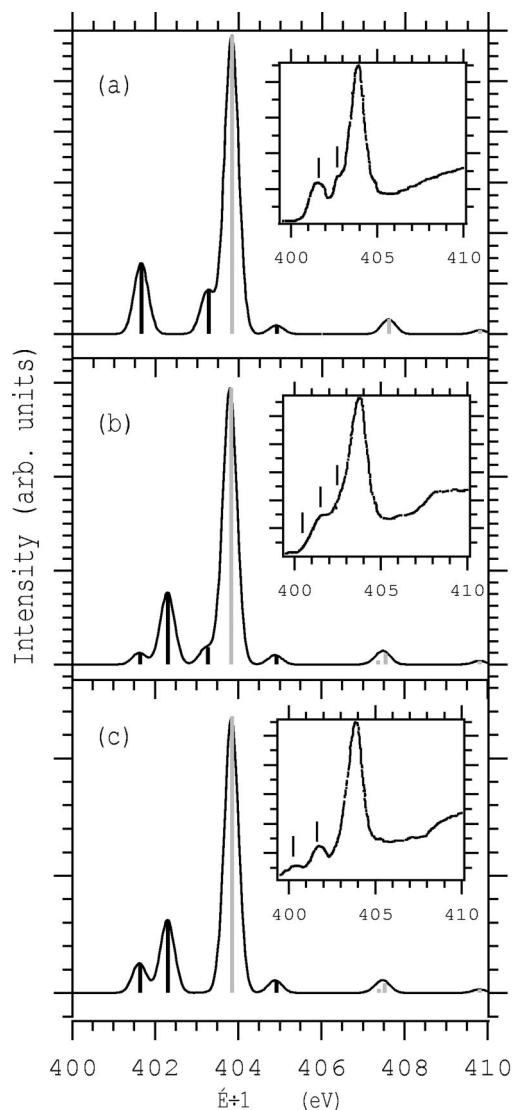


FIG. 6. The calculated N 1s x-ray absorption spectra for (a) pNA, (b) mNA, (c) oNA. The black and gray lines correspond to transitions from the N(1) 1s and N(8) 1s core electron to the unoccupied antibonding MOs, respectively. Experimental spectra (Ref. 22) are shown in the inset.

where  $|\Psi_{\xi}\rangle$  is the global eigenstate of the single-core-excited state, and  $\xi$  is an index for the eigenstate. The middle and right columns in Fig. 7 show  $\rho^{\xi}$  for the N(1) and N(8) single-core excited states, respectively.

Similarities of the left and middle columns, together with the almost identical level spacings between these states as shown in Table II, suggest that the N(1) core hole does not effect the electronic states of the antibonding MOs, i.e., the core excitonic effect is very weak for the N(1) core excitation. This is because the small N(1)  $2p_z$  AO component is involved in the antibonding MOs. The intensity distribution among the 4 black line spectra corresponds to the N(1)  $2p_z$  AO component of each core excited state: the transition to the 2nd N(1) core excited states (f) is the strongest because this state has the largest N(1)  $2p_z$  AO component among the N(1) core excited states. On the other hand, the level separations and the density matrix for the N(8) core excited state are very different from the ground state (see Fig. 7 and Table

II), suggesting a strong core excitonic effect in this case. The 1st N(8) core excited state (h) is strongly localized on NO<sub>2</sub> group, while for the other excited states [(i) to (l)] the excited electron is more delocalized. Since the absorption strength is determined by the N(8)  $2p_z$  AO component, the lowest peak carries most intensity and is well separated from the other weak lines, as seen in Fig. 6.

Our calculations reproduce well the experimental spectra shown in the inset,<sup>22</sup> especially the pre-edge spectral structures below the main peak at 404 eV. Above the main peak, the transitions to the more delocalized  $\sigma$  orbitals and to the continuum states give the broad background in the experiment. These are not included in our model.

We next compare the spectra of the three isomers. As indicated in Sec. III, the core exciton effect is weak in the N(1) core excited state. The excited core electron is delocalized over the entire molecule, so that the N(1) 1s absorption lines (black) in Fig. 6 are sensitive to the structural change of the isomers.

In mNA, the absorption line to the second N(1) core excited state is the strongest among the N(1) 1s absorption lines (black), because it has the largest N(1)  $2p_z$  AO component as mentioned in Sec. III. The N(1)  $2p_z$  AO component for each state is determined by the hybridization strength between the N(1)  $2p_z$  and its nearest neighbor C  $2p_z$  AO at the site 4. As found from Fig. 4, the second excited state has the largest N(1)  $2p_z$  AO component by this hybridization between the C  $2p_z$  AO at the site 4 and N(1)  $2p_z$  AO.

In pNA, the NH<sub>2</sub> group is bonded with the C atom at the site 2. In this case the hybridization between the N(1)  $2p_z$  AO at site 2 and the C  $2p_z$  AO at the site 2 becomes large for the first, third, and fourth excited state, while there is no hybridization for the second excited state. As a result, the N(1) 1s absorption transition is allowed for these three states, and is forbidden for the second excited state. For the same reason, the first, second, and fourth excited states are active for the N(1) 1s absorption, while the third excited state is dark.

In contrast, the core exciton effect is large for the N(8) 1s core excitation, so that the excited core electron is strongly localized NO<sub>2</sub> group, and is not affected by the difference of the position of NH<sub>2</sub> group. Consequently, the transition to the N(8) 1s core exciton absorption dominates the other transition, and the absorption line spectra (gray) are insensitive to the structural change of the isomers.

Since the distribution of absorption line intensities reflects the N  $2p_z$  AO component for each core excited state, we do not get any information on the degree of delocalization of the core excited state without a theoretical analysis based on an appropriate model. It will be shown below that x-ray pump-probe spectroscopy, in contrast, directly provides this information.

#### IV. THE X-RAY PUMP-PROBE SPECTRUM

In a pump-probe experiment the molecule is subjected to two beams: the pump ( $\mathbf{k}_1, \omega_1$ ) and probe ( $\mathbf{k}_2, \omega_2$ ). The signal given by the difference in the probe absorption with

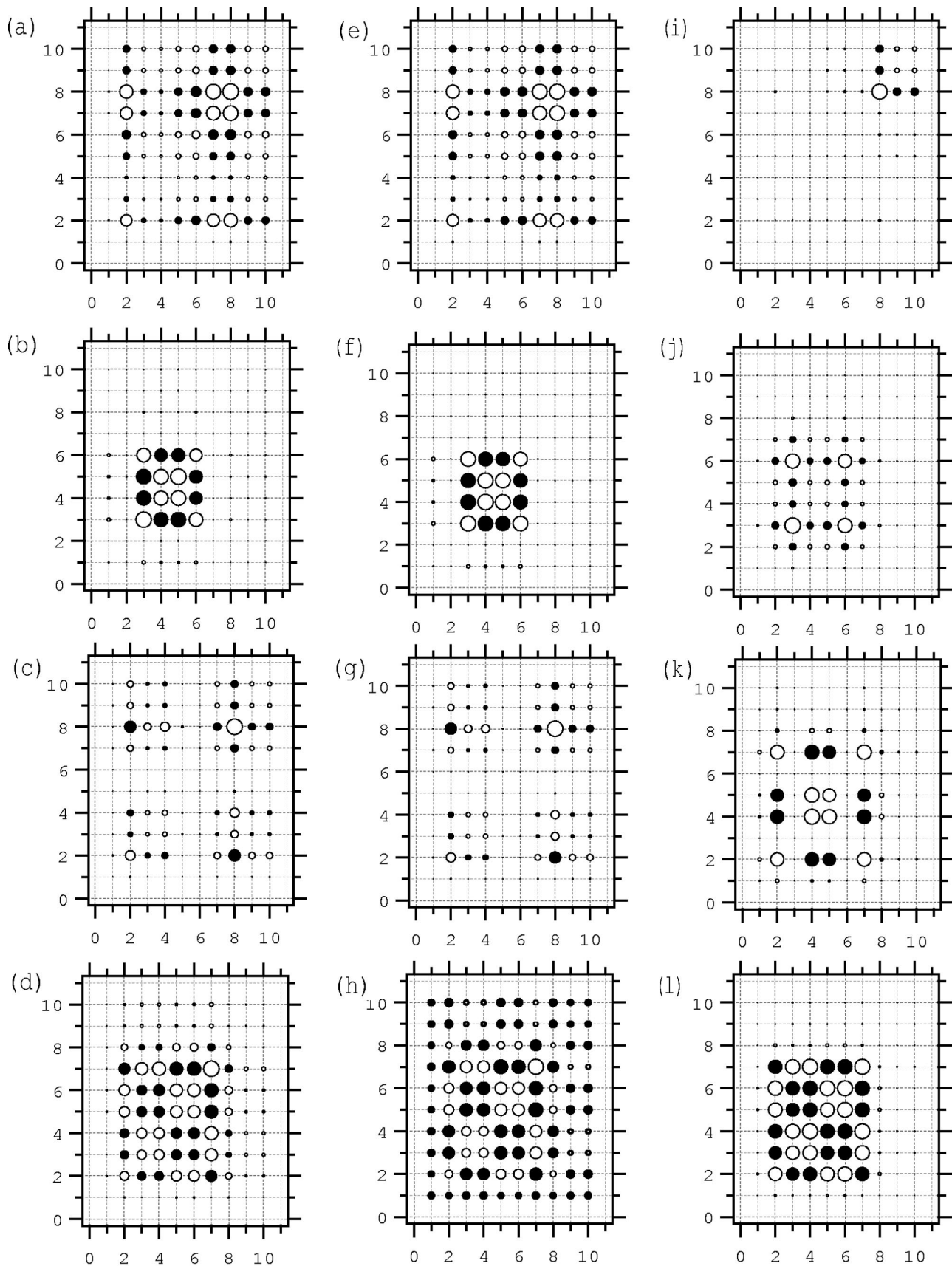


FIG. 7. Density matrices for the ground state [Eq. (13)] and the single-core excited states for mNA: (a)–(d) ground state, (e)–(h) N(1)  $1s$  ( $\text{NH}_2$ ) core excited states, and (i)–(l) N(8)  $1s$  ( $\text{NO}_2$ ) core excited states. Open circles: positive; solid circles: negative. The circle radius is proportional to the corresponding density matrix element.

TABLE II. The energies of the antibonding MOs, N(1) 1s, and N(8) 1s single-core-excited states in mNA (in eV). The energy differences from the lowest state are listed in parentheses.

MO ( $\alpha$ )		N(1) 1s		N(8) 1s	
-1.23		401.65		403.83	
-0.49	(0.74)	402.31	(0.66)	407.37	(3.54)
0.39	(1.62)	403.27	(1.62)	407.54	(3.71)
2.04	(3.27)	404.92	(3.27)	409.86	(6.03)

and without the pump is a special case of heterodyne-detected four-wave mixing with three modes of the incoming fields,<sup>9</sup>

$$W_{PP}(\mathbf{k}_1, \omega_1, \mathbf{k}_2, \omega_2) \propto \omega_2 \text{Im} E_2^* P^{(3)}(\mathbf{k}_2, \omega_2) / |E_2|^2 \propto \text{Im} \chi^{(3)}(-\mathbf{k}_2, -\omega_2; \mathbf{k}_1, \omega_1, -\mathbf{k}_1, -\omega_1, \mathbf{k}_2, \omega_2). \quad (15)$$

General formal expressions for the frequency and wave vector dependent third order susceptibility  $\chi^{(3)}$  are presented in Appendix A. The Liouville space pathways showing the various contributions to x-ray four-wave mixing under the rotating wave approximation (RWA) for the three band core exciton model shown in Fig. 5 are given in Appendix B. Explicit expressions for x-ray pump-probe spectra with two incoming fields, which is a special case of Appendix B, are given in Eqs. (C2) and (C3).

The x-ray wavelength corresponding to the N 1s core excitation to the antibonding  $\pi$  orbitals ( $\sim 400$  eV) is about 30 Å, this is long compared to atomic distances which justifies using the long wavelength limit, setting  $\mathbf{k}=0$ . Two-dimensional plots of the calculated x-ray pump-probe spectra for pNA, mNA, and oNA are shown in Figs. 8(a), 9(a), and 10(a), respectively. The horizontal (vertical) axis is the probe (pump) frequency.

The spectra have negative photobleaching (PB) signals (red) attributed to the Liouville space pathways (I)–(IV). The PB signal has two contributions, the stimulated emission Liouville space [pathways (I) and (II)] and the hole burning [pathways (III) and (IV)]. In addition, we see positive excited state absorption (ESA) signals (blue) attributed to pathways (V)–(VII). The sum of contributions  $R_I, R_{II}, R_{III},$  and  $R_{IV}$  [(C1a) to (C1d)] is shown in panels (b), the sum of contributions  $R_V, R_{VI},$  and  $R_{VII}$  [(C1e) to (C1g)] is shown in panels (c).

Since  $\Gamma_{gg}$  in the denominator of  $I_{gg}(\omega)$  in  $W^{III}$  and  $W^{IV}$  is much smaller than  $\Gamma_{eg}$  or  $\Gamma_{e'e'}$  in  $I_{eg}(\omega)$  or  $I_{e'e'}(\omega)$  in  $W^{II}$  [see Eqs. (C3)], the dominant contributions come from  $W^{III}$  and  $W^{IV}$  corresponding to pathways (III) and (IV),

$$W^{III} = - \sum_{ee'} J_{eg;eg}(\mathbf{0}) J_{ge;e'g}^*(\mathbf{0}) \{ I_{eg}(\omega_2) I_{gg}(0) I_{e'e'}(-\omega_1) + I_{eg}(\omega_2) I_{gg}(\omega_2 - \omega_1) I_{e'e'}(-\omega_1) \}, \quad (16)$$

$$W^{IV} = \sum_{ee'} J_{ge';e'g}(\mathbf{0}) J_{ge;eg}(\mathbf{0}) \{ I_{e'g}(\omega_2) I_{gg}(0) I_{eg}(\omega_1) + I_{e'g}(\omega_2) I_{gg}(\omega_2 - \omega_1) I_{eg}(\omega_2) \}. \quad (17)$$

Since  $I_{gg}(0)$  is large, the first terms in  $W^{III}$  and  $W^{IV}$  dominate the signal. The  $\omega_1$  and  $\omega_2$  dependence of the first terms is factorized, indicating the lack of correlations between  $\omega_1$  and  $\omega_2$ . The simple product of  $I_{eg}(\omega_2)$  and  $I_{eg}(\omega_1)$  in the first terms of  $W^{III}$  and  $W^{IV}$  gives the sharp resonant (negative) peak when either  $\omega_1$  or  $\omega_2$  is resonant with the transition energy from the ground to one of the single-core excited states. On the other hand, in the second terms  $\omega_1$  and  $\omega_2$  are correlated through  $I_{gg}(\omega_2 - \omega_1)$ , which gives a negative sharp peak for  $\omega_2 = \omega_1$ .

The pump-probe spectra of mNA are depicted in Fig. 11 where the pump is tuned to the N 1s x-ray absorption peaks in Fig. 6: (a)  $\omega_1 = 401.65$  eV, (b) 402.31 eV, (c) 403.27 eV, and (d) 404.92 eV. Sharp dips appear at same position of the x-ray absorption spectra with the same intensity ratio of the x-ray absorption spectra, except for the peak at  $\omega_2 = \omega_1$  shown by the arrows in Fig. 11. Similar spectra were obtained for pNA and oNA (not shown).

We next turn to the contribution of the ESA in (c) in Figs. 8, 9, and 10, for the three isomers. These positive peaks have characteristically different correlations between  $\omega_1$  and  $\omega_2$  compared to the bleaching signal: The peak positions shift to satisfy energy conservation,  $\omega_1 = E_e - E_g$  and  $\omega_1 + \omega_2 = E_f - E_g$ .

By tuning the pump to excite the N(1) 1s core electron and the probe to excite the N(8) 1s core electron, we find that the spectra are sensitive to the degree of delocalization of the electron excited by the pump. If it is strongly localized at N(1), the pump-excitation should not affect the probe absorption at N(8); the probe absorption spectra resembles the N(8) 1s linear absorption lines. The rectangular area in (c) of Figs. 8, 9, and 10 corresponds to this case. The horizontal dotted lines represent the energy of the N(1) 1s absorption lines, the black line spectra in Fig. 6, i.e., where the first resonance condition  $\omega_1 = E_e - E_g$  is satisfied. The dashed lines represent the correlation between  $\omega_1$  and  $\omega_2$  where the second resonance condition  $\omega_1 + \omega_2 = E_f - E_g$  is satisfied. Each of the dashed lines labeled A to D represents a family of resonances with a common final state.

Sections of the spectra of Fig. 9(d) for mNA at the N(1) 1s resonant excitation energies are shown in Fig. 12, for (a)  $\omega_1 = 401.65$  eV, (b) 402.31 eV, (c) 403.27 eV, (d) 404.92 eV. The labels A–D correspond to lines A–D in Fig. 9. In (a) there are two large positive peaks (A and B), and in (b) the peak A disappears and only B remains. The peak structures of A and B show up in (c), and in (d) only peak C has a strong positive intensity.

In order to interpret the excitation energy dependence, let us revisit the density matrix plots of mNA shown in Fig. 7. Figures 7(e) and 7(g) suggest that in the 1st and 3rd N(1) core-excited states the excited electron is coherently delocalized over N(8), while in the 2nd N(1) excited state (f) it is localized within the benzene ring. In the 4th N(1) excited state (h) the excited electron is almost localized within the benzene ring, and there is a small degree of correlation between the benzene  $\pi^*$  state and the antibonding  $\pi^*$  ( $\text{NO}_2$ ) states. When the N(1) 1s core electron is excited to the 1st core excited state (e), the N(8)  $2p_z$  AO is strongly occupied, so that the N 1s core excitation to the localized core exciton

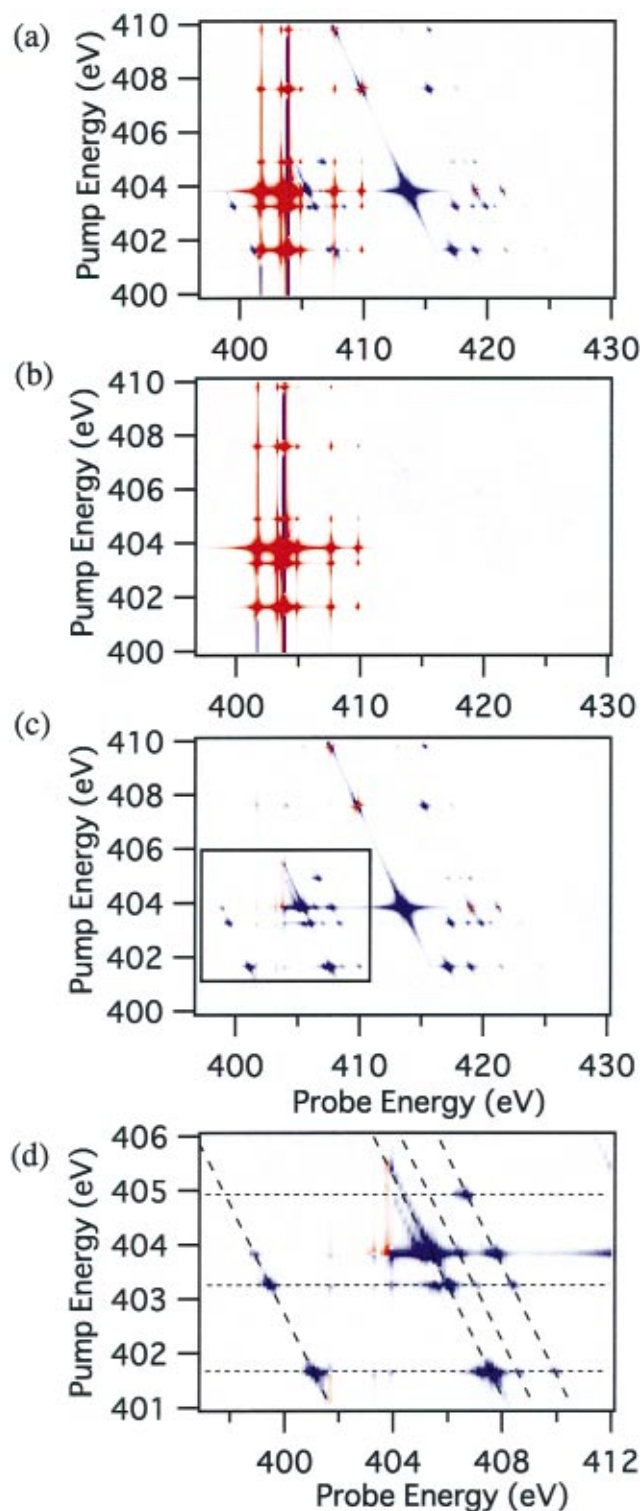


FIG. 8. (Color) Calculated x-ray pump-probe spectra of pNA. The horizontal and vertical axes are the probe and pump frequencies, respectively. Negative and positive signals are depicted by red and blue images, respectively. (a)  $W_{PP}$ , (b) the sum of the contributions of Liouville pathways I-IV, (c) the sum of the contributions of Liouville pathways V-VII. (d) Same as panel (c) but on an expanded scale.

state on the N(8) is suppressed by Pauli exclusion and these excited electrons have strong Coulomb interactions, causing the two peak structures of A and B.

When the N(1) 1s core electron is excited to the second excited state (f), the N(8)  $2p_z$  AO remains unoccupied, so

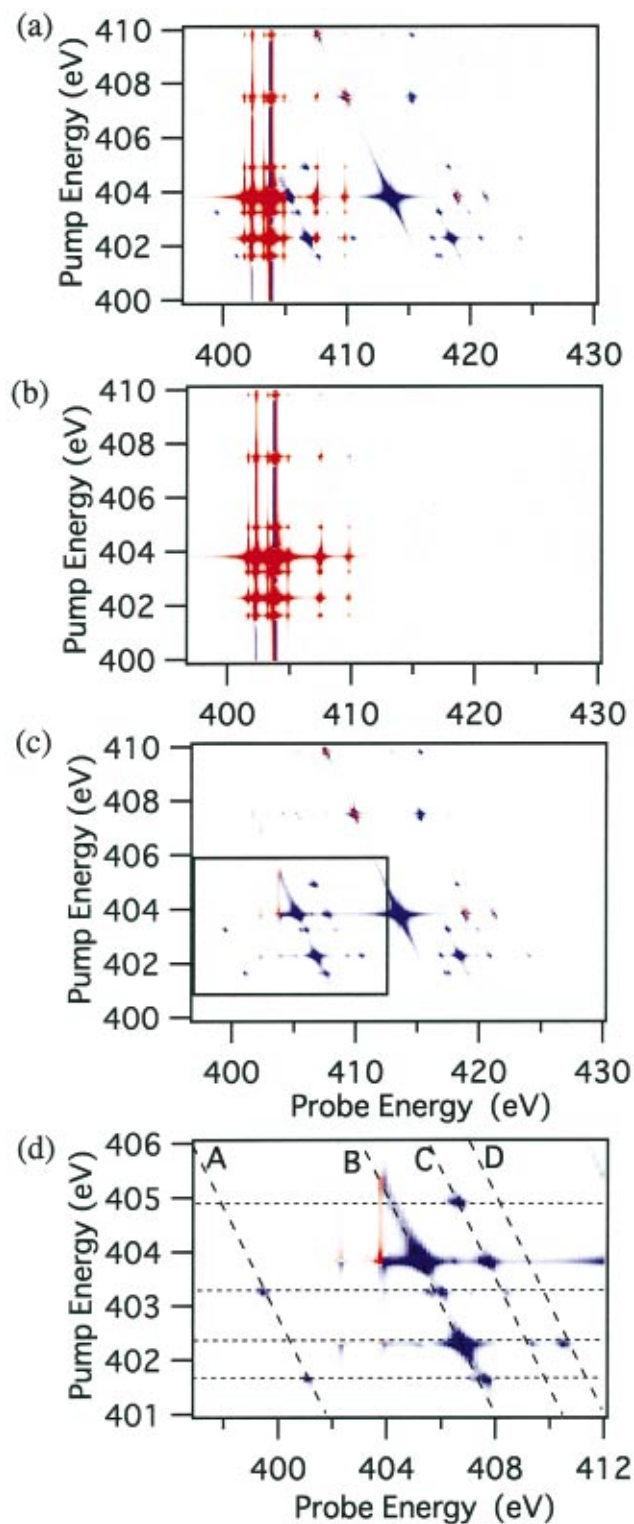


FIG. 9. (Color) Same as Fig. 8, but for mNA.

that the N(8) 1s core electron is excited to the strongly localized core exciton state on N(8): the pump x-ray beam does not effect the N(8) 1s x-ray absorption process. We therefore see a single intense peak corresponding to the intense red line at 403.84 eV in Fig. 6.

The situation is the same when the N(1) 1s core electron is excited to the third core excited state (g) as in the case of the excitation to the first peak (e). The two peak structures A

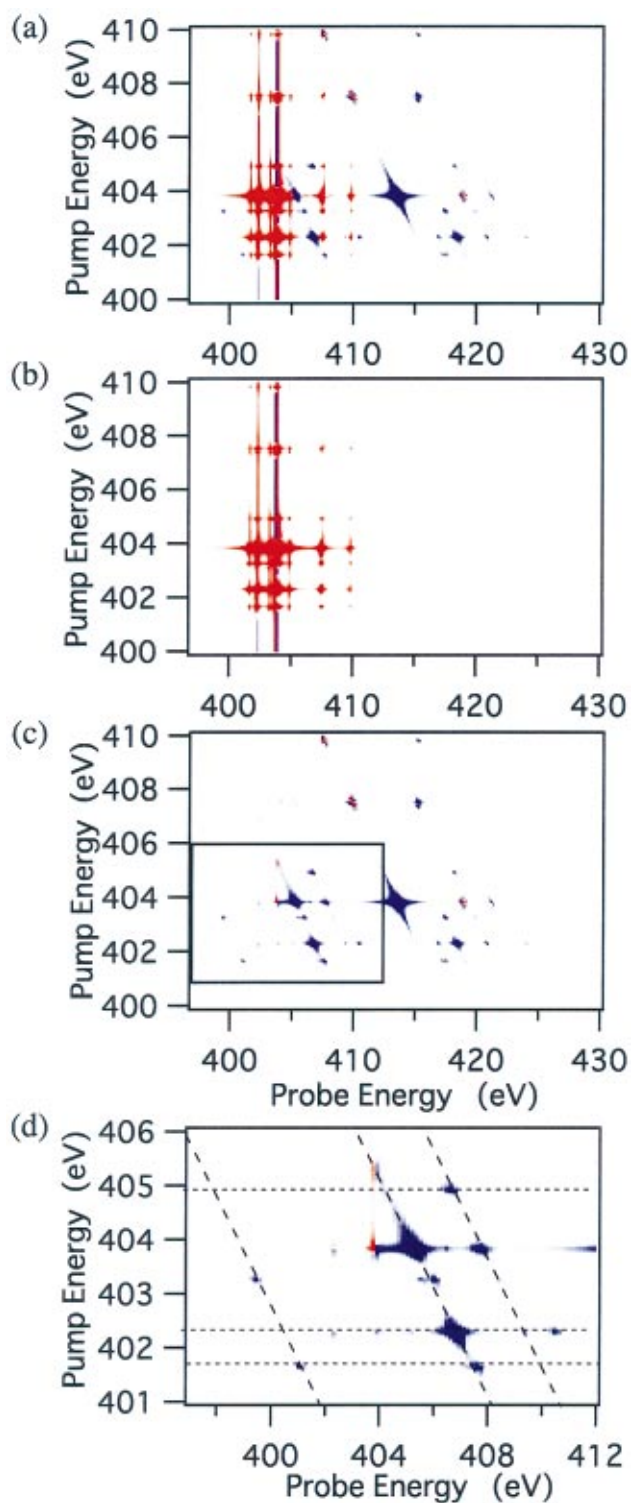


FIG. 10. (Color) Same as Fig. 8, but for oNA.

and B thus appear. For the 4th N(1)  $1s$  excited state (h), the population of the N(8)  $2p_z$  AO is small, so that the N(8)  $1s$  core electron is excited to create the core exciton on N(8) as in case (f).

The differences in the 2D pump-probe spectra of the various isomers are related to the difference of the single exciton  $\omega_1$  resonances. For example, the strong  $\omega_1 = 402.31$  eV resonance of mNA is absent in pNA. And the

probe resonances for the  $\omega_1 = 403.84$  eV pump excitation in mNA do not appear in oNA. These differences are attributed to the different x-ray absorption of the N(1) site among these isomers, as shown by the solid lines in Fig. 6. For the same pump frequency, the probe spectra have almost the same profile for all isomers, because the electronic structure of the corresponding excited states are essentially the same.

## V. CONCLUSIONS

In this paper we applied the general expressions for the frequency and wave vector dependent  $\chi^{(3)}$  (Ref. 7) to calculate the x-ray pump-probe spectra of the three isomers of nitroaniline using the core exciton model with the four unoccupied MO for the  $\pi$  system and two N  $1s$  core orbitals. We took into account the core exciton effect and the Coulomb interactions between the excited electrons and core holes.

The calculated N  $1s$  x-ray absorption spectra are in good agreement with experiment. The x-ray pump-probe spectra have PB and ESA components showing different types of correlations between  $\omega_1$  and  $\omega_2$ : while there is no correlation in PB, they are strongly correlated to satisfy the resonant conditions of  $\omega_1 = E_e - E_g$  and  $\omega_1 + \omega_2 = E_f - E_g$  in ESA.

We further showed that while x-ray absorption reflects the N  $2p_z$  AO component for the core excited state, the ESA signal, where the pump excites the N(1)  $1s$  core electron, and the N(8)  $1s$  core electron is excited by probe, contains direct signatures of the excited electron delocalization: When the N(1)  $1s$  core electron is excited to the state that coherently extends over the N(8) site the N(8)  $1s$  absorption is strongly effected by the pump-excitation, while the N(1)  $1s$  core excited is localized N(8)  $1s$  absorption resembles the linear absorption spectrum without the pump.

In the  $1s$  core excitation of nitrogen, the x-ray wavelength is about  $30 \text{ \AA}$ , which justifies taking the long wavelength limit and setting  $\mathbf{k} = \mathbf{0}$ . But when the x-ray wavelength is comparable to the size of the molecule or atomic distance, the x-ray four-wave mixing signal should depend explicitly on the wave vectors of the x-ray fields. Recent experiments on the inelastic resonant x-ray emission for the K-edge in  $3d$  transition metal compounds,<sup>26-28</sup> and Si K-edge resonant x-ray emission<sup>29</sup> have revealed an interesting wave vector dependence. So far, there has been no report on the wave vector dependence of molecular x-ray spectroscopies. We expect strong  $\mathbf{k}$ -dependence when the distance between the core excited sites is comparable to the x-ray wavelength. The wave vector dependence of x-ray four-wave mixing should provide detailed information on the spatially nonlocal nature of the response.

The core exciton model used in this paper is similar to the two-band model of optical excitation of semiconductors where the transfer of the hole is taken into account.<sup>30,31</sup> Using the localization of core holes and the characteristic energy for each core orbital, we can map the delocalized valence states onto each atomic component. Other techniques can select a particular atomic component from the congested valence occupied, unoccupied, and the valence excited states.<sup>4,32,33</sup> These include resonant photoemission, resonant x-ray emission. In resonant bremsstrahlung isochromat spec-

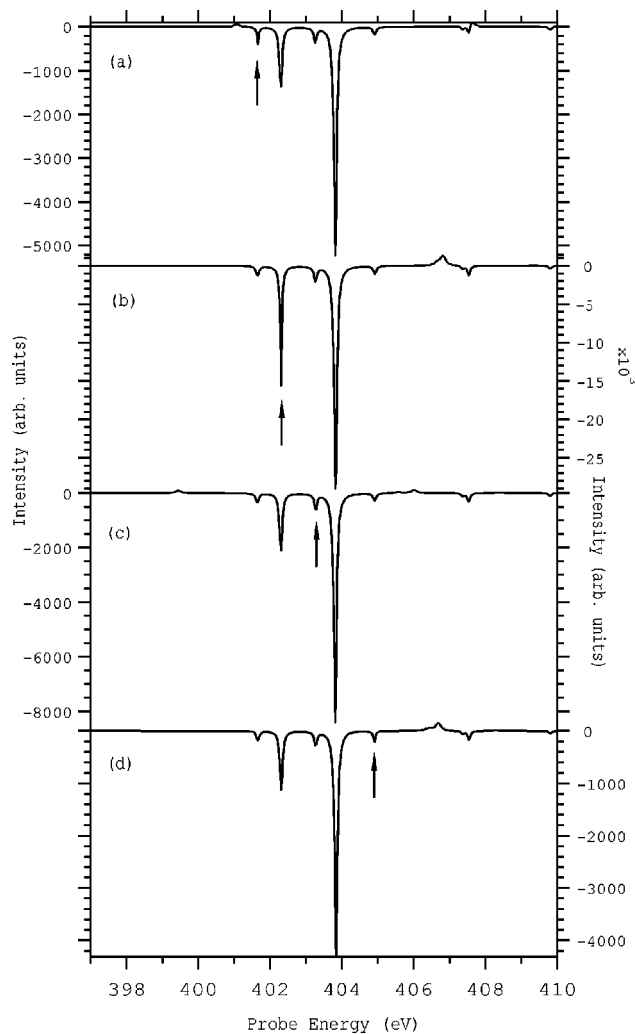


FIG. 11. X-ray pump-probe spectra when the pump frequency, (marked by an arrow) is tuned at N 1s x-ray absorption peaks in Fig. 6: (a)  $\omega_1 = 401.65$  eV, (b) 402.31 eV, (c) 403.27 eV, and (d) 404.92 eV.

troscopies (BIS), known also as inverse photoemission, a high energy electron is trapped in an unoccupied orbital and the excess energy is released as a photon. The signal is obtained by detecting the photon at a fixed frequency and scanning the incident electron energy. Thus x-ray four-wave mixing can map  $\chi^{(3)}$  onto each atomic contribution allowing to pinpoint the origin of electronic excitations of molecules.

Finally we note the dephasing rate  $\Gamma_{ab}$  is generally given by the sum of the inverse lifetimes  $\gamma_a$  and  $\gamma_b$  of the  $a$  and  $b$  states, and the pure dephasing rate  $\hat{\Gamma}_{ab}$  for the  $ab$  transition,<sup>34</sup>

$$\Gamma_{ab} = \frac{1}{2}(\gamma_a + \gamma_b) + \hat{\Gamma}_{ab}. \quad (18)$$

In the present calculations, we used  $\gamma_e = 92$  meV as estimated by McGuire<sup>35</sup> and  $\gamma_f = 2\gamma_e$ , and neglected the pure dephasing and set  $\hat{\Gamma}_{ab} = 0$  (Table I). For  $\gamma_g$ , we used a finite small value of 10 meV. This eliminates a divergence of  $I_{gg}(\omega)$  in degenerate four-wave mixing.<sup>9</sup> In x-ray spectroscopies, it has long been assumed that, since the nonradiative Auger decay lifetime is very short ( $\leq 10$  fs), lifetime broadening dominates the absorption linewidth, and pure

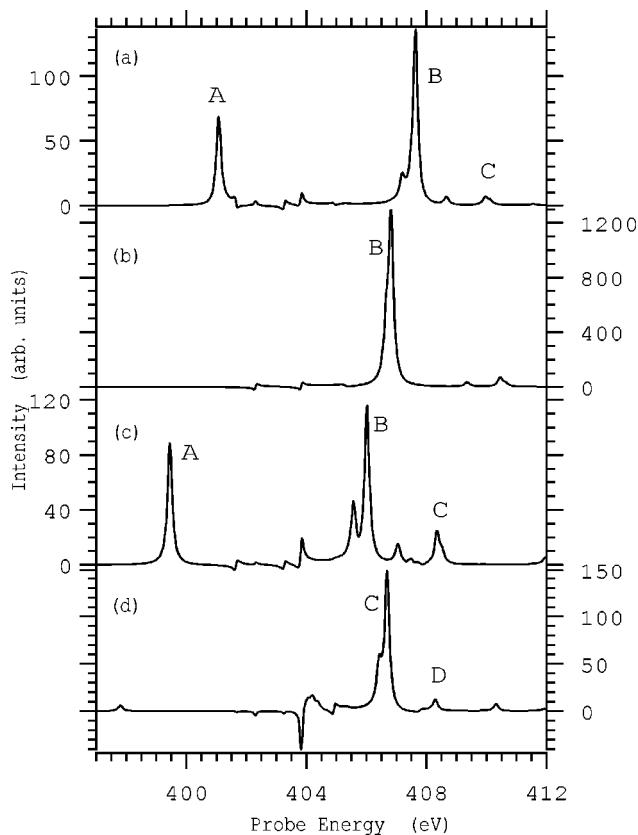


FIG. 12. Sections of the x-ray pump-probe spectra of mNA in the rectangular area in Fig. 9. The pump energies are (a)  $\omega_1 = 401.65$  eV, (b) 402.31 eV, (c) 403.27 eV, and (d) 404.92 eV.

dephasing may be neglected. But in some molecules with a strong electron-vibration coupling in the core excited state,<sup>36-39</sup> the absorption linewidth may become larger than expected from the Auger autoionization lifetime, and pure dephasing processes can be important. This interesting subject should be investigated further.

We have calculated the time-resolved resonant x-ray emission spectrum for a one-dimensional molecular chain and showed how the dynamics of the relative motion of the core exciton is clearly revealed.<sup>8</sup> This requires  $\leq 1.0$  fs time resolution. Time-resolved x-ray four-wave-mixing spectroscopy should also provide useful information on the electron dynamics in molecules: For example, the dynamical exciton transfer from site to site,<sup>40</sup> dynamics of polaron formation by electron-phonon interaction,<sup>41-43</sup> and dissociation dynamics following the core excitation can be observed by snapshots of the nonlinear x-ray response.

## ACKNOWLEDGMENTS

The authors gratefully acknowledge the support of the National Science Foundation. The numerical calculations were performed in the supercomputing center at Osaka University.

## APPENDIX A: THE FREQUENCY AND WAVE VECTOR DEPENDENT $\chi^{(3)}$

Below we give the general expression for the third order nonlinear susceptibility  $\chi^{(3)}$ . The four-wave mixing experiment involves three modes of the incoming field,

$$E(\mathbf{r}, t) = \sum_{j=1}^3 [E_j \exp[i\mathbf{k}_j \cdot \mathbf{r} - i\omega_j t] + E_j^* \exp[-i\mathbf{k}_j \cdot \mathbf{r} + i\omega_j t]]. \quad (\text{A1})$$

The third order nonlinear polarization at a point  $\mathbf{r}$  at time  $t$  is <sup>7</sup>

$$P^{(3)}(\mathbf{r}, t) = \int d\mathbf{r}_3 \int d\mathbf{r}_2 \int d\mathbf{r}_1 \int dt_3 \times \int dt_2 \int dt_1 \cdot \mathcal{S}^{(3)}(\mathbf{r}; \mathbf{r}_3 \mathbf{r}_2 \mathbf{r}_1 t_3 t_2 t_1) E(\mathbf{r}_3, t-t_3) \times E(\mathbf{r}_2, t-t_3-t_2) E(\mathbf{r}_1, t-t_3-t_2-t_1). \quad (\text{A2})$$

Fourier transformation to  $\omega$ ,  $\mathbf{k}$  space gives

$$P^{(3)}(\mathbf{k}_s, \omega_s) \equiv \int d\mathbf{r} \int dt P^{(3)}(\mathbf{r}, t) \exp[-i\mathbf{k}_s \cdot \mathbf{r} + i\omega_s t] = 2\pi E_3 E_2 E_1 \mathcal{S}^{(3)}(-\mathbf{k}_s; \mathbf{k}_3, \mathbf{k}_2, \mathbf{k}_1, \omega_3 + \omega_2 + \omega_1, \omega_2 + \omega_1, \omega_1), \quad (\text{A3})$$

where  $\omega_s \equiv \omega_1 + \omega_2 + \omega_3$  and  $\mathbf{k}_s \equiv \mathbf{k}_1 + \mathbf{k}_2 + \mathbf{k}_3$ . In Eq. (A3),  $\mathcal{S}^{(3)}(-\mathbf{k}_s; \mathbf{k}_3, \mathbf{k}_2, \mathbf{k}_1, \omega_3, \omega_2, \omega_1)$  is defined as the multidimensional Fourier transform of  $\mathcal{S}^{(3)}(\mathbf{r}; \mathbf{r}_3 \mathbf{r}_2 \mathbf{r}_1 t_3 t_2 t_1)$ ,

$$\mathcal{S}^{(3)}(-\mathbf{k}_s; \mathbf{k}_3, \mathbf{k}_2, \mathbf{k}_1, \omega_3, \omega_2, \omega_1) \equiv \int d\mathbf{r} \int d\mathbf{r}_3 \int d\mathbf{r}_2 \int d\mathbf{r}_1 \int dt_3 \int dt_2 \int dt_1 \times \mathcal{S}^{(3)}(\mathbf{r}; \mathbf{r}_3 \mathbf{r}_2 \mathbf{r}_1 t_3 t_2 t_1) \cdot \exp[-i\mathbf{k}_3 \cdot (\mathbf{r} - \mathbf{r}_3) - i\mathbf{k}_2 \cdot (\mathbf{r} - \mathbf{r}_2) - i\mathbf{k}_1 \cdot (\mathbf{r} - \mathbf{r}_1)] \times \exp[i\omega_3 t_3 + i\omega_2 t_2 + i\omega_1 t_1]. \quad (\text{A4})$$

Taking into account the invariance of the permutations of  $(\mathbf{k}_j, \omega_j)$  ( $j=1,3$ ) in Eq. (A3), the third order nonlinear susceptibility is

$$\chi^{(3)}(-\mathbf{k}_s, -\omega_s; \mathbf{k}_1, \omega_1, \mathbf{k}_2, \omega_2, \mathbf{k}_3, \omega_3) = \frac{\nu_0}{3!} \sum_p \mathcal{S}^{(3)}(-\mathbf{k}_s; \mathbf{k}_3, \mathbf{k}_2, \mathbf{k}_1, \omega_3, \omega_2, \omega_1), \quad (\text{A5})$$

where  $\nu_0$  is a density of noninteracting molecules and  $\sum_p$  is a sum over the six permutations of  $(\mathbf{k}_1, \omega_1)$ ,  $(\mathbf{k}_2, \omega_2)$ , and  $(\mathbf{k}_3, \omega_3)$ .

The nonlinear response function for the current density  $\mathcal{S}^{(3)}$  is given by

$$\mathcal{S}^{(3)}(\mathbf{r}; \mathbf{r}_3, \mathbf{r}_2, \mathbf{r}_1, t_3, t_2, t_1) = \frac{i}{\hbar^3} \theta(t_1) \theta(t_2) \theta(t_3) (\omega_1 \omega_2 \omega_3 \omega_s)^{-1} \langle \hat{j}(\mathbf{r}, t_3 + t_2 + t_1) \times [\hat{j}(\mathbf{r}_3, t_2 + t_1), [\hat{j}(\mathbf{r}_2, t_1), [\hat{j}(\mathbf{r}_1, 0), \rho(-\infty)]]] \rangle = \frac{i}{\hbar^3} \theta(t_1) \theta(t_2) \theta(t_3) (\omega_1 \omega_2 \omega_3 \omega_s)^{-1} \times \sum_{\alpha=1}^4 [R_{\alpha}(\mathbf{r}; \mathbf{r}_3, \mathbf{r}_2, \mathbf{r}_1, t_3, t_2, t_1) - R_{\alpha}^*(\mathbf{r}; \mathbf{r}_3, \mathbf{r}_2, \mathbf{r}_1, t_3, t_2, t_1)]. \quad (\text{A6})$$

Each  $R_j$  ( $j=1-4$ ) is given by a four point correlation functions representing a distinct Liouville space pathway,

$$R_1 = \langle \hat{j}(\mathbf{r}_2, t_1) \hat{j}(\mathbf{r}_3, t_1 + t_2) \hat{j}(\mathbf{r}, t_1 + t_2 + t_3) \hat{j}(\mathbf{r}_1, 0) \rangle, \quad (\text{A7a})$$

$$R_2 = \langle \hat{j}(\mathbf{r}_1, 0) \hat{j}(\mathbf{r}_3, t_1 + t_2) \hat{j}(\mathbf{r}, t_1 + t_2 + t_3) \hat{j}(\mathbf{r}_2, t_1) \rangle, \quad (\text{A7b})$$

$$R_3 = \langle \hat{j}(\mathbf{r}_1, 0) \hat{j}(\mathbf{r}_2, t_1) \hat{j}(\mathbf{r}, t_1 + t_2 + t_3) \hat{j}(\mathbf{r}_3, t_1 + t_2) \rangle, \quad (\text{A7c})$$

$$R_4 = \langle \hat{j}(\mathbf{r}, t_1 + t_2 + t_3) \hat{j}(\mathbf{r}_3, t_1 + t_2) \hat{j}(\mathbf{r}_2, t_1) \hat{j}(\mathbf{r}_1, 0) \rangle. \quad (\text{A7d})$$

Note a slight difference in notation:  $R_3$  and  $R_4$  are identical to those given in Eqs. (29) in Ref. 7, however  $R_1$  and  $R_2$  are equal to  $-R_1^*$  and  $-R_2^*$  of the reference.

Substituting Eq. (A6) into Eq. (A4), we obtain

$$\mathcal{S}^{(3)}(-\mathbf{k}_s; \mathbf{k}_3, \mathbf{k}_2, \mathbf{k}_1, \omega_3, \omega_2, \omega_1) = \frac{1}{\hbar^3 (\omega_1 \omega_2 \omega_3 \omega_s)} \sum_{\alpha=1}^4 [R_{\alpha}(-\mathbf{k}_s; \mathbf{k}_3, \mathbf{k}_2, \mathbf{k}_1, \omega_3, \omega_2, \mathbf{k}_1, \omega_1) + R_{\alpha}^*(\mathbf{k}_s; -\mathbf{k}_3, -\mathbf{k}_2, -\mathbf{k}_1, -\omega_3, -\omega_2, -\omega_1)], \quad (\text{A8})$$

where the response function in the frequency domain is defined similar to Eq. (A4) by

$$R_{\alpha}(-\mathbf{k}_s; \mathbf{k}_3, \mathbf{k}_2, \mathbf{k}_1, \omega_3, \omega_2, \omega_1) \equiv (-i)^3 \int d\mathbf{r} \int d\mathbf{r}_3 \int d\mathbf{r}_2 \int d\mathbf{r}_1 \int_0^{\infty} dt_3 \int_0^{\infty} dt_2 \int_0^{\infty} dt_1 R_{\alpha}(\mathbf{r}; \mathbf{r}_3 \mathbf{r}_2 \mathbf{r}_1 t_3 t_2 t_1) \cdot \exp[-i\mathbf{k}_3 \cdot (\mathbf{r} - \mathbf{r}_3) - i\mathbf{k}_2 \cdot (\mathbf{r} - \mathbf{r}_2) - i\mathbf{k}_1 \cdot (\mathbf{r} - \mathbf{r}_1)] \exp[i\omega_3 t_3 + i\omega_2 t_2 + i\omega_1 t_1]. \quad (\text{A9})$$

From Eqs. (A7) and (A9), we have

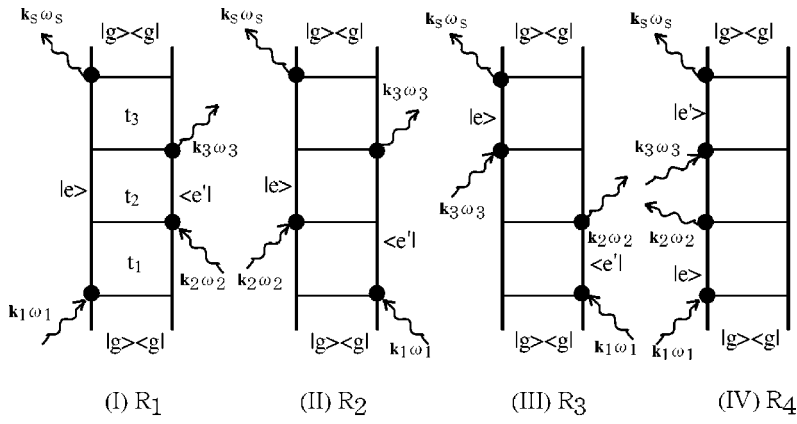
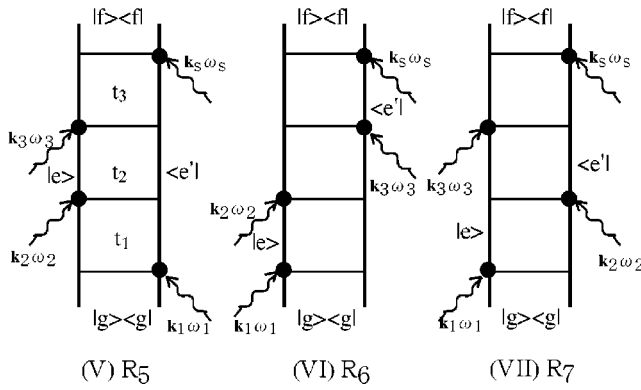


FIG. 13. Liouville space pathways for x-ray pump-probe spectroscopy which survive the RWA. PB: (I)–(IV), and ESA: (V)–(VII).



$$R_1(-\mathbf{k}_s; \mathbf{k}_3, \mathbf{k}_2, \mathbf{k}_1, \omega_3, \omega_2, \omega_1) = \sum_{abcd} P(a) \int d\mathbf{r} \int d\mathbf{r}_3 \int d\mathbf{r}_2 \int d\mathbf{r}_1 j_{cd}(\mathbf{r}) j_{da}(\mathbf{r}_1) j_{ab}(\mathbf{r}_2) j_{bc}(\mathbf{r}_3) \cdot \exp[-i\mathbf{k}_3 \cdot (\mathbf{r} - \mathbf{r}_3) - i\mathbf{k}_2 \cdot (\mathbf{r} - \mathbf{r}_2) - i\mathbf{k}_1 \cdot (\mathbf{r} - \mathbf{r}_1)] I_{dc}(\omega_3) I_{db}(\omega_2) I_{da}(\omega_1), \quad (\text{A10a})$$

$$R_2(-\mathbf{k}_s; \mathbf{k}_3, \mathbf{k}_2, \mathbf{k}_1, \omega_3, \omega_2, \omega_1) = \sum_{abcd} P(a) \int d\mathbf{r} \int d\mathbf{r}_3 \int d\mathbf{r}_2 \int d\mathbf{r}_1 j_{cd}(\mathbf{r}) j_{da}(\mathbf{r}_1) j_{ab}(\mathbf{r}_2) j_{bc}(\mathbf{r}_3) \cdot \exp[-i\mathbf{k}_3 \cdot (\mathbf{r} - \mathbf{r}_3) - i\mathbf{k}_2 \cdot (\mathbf{r} - \mathbf{r}_2) - i\mathbf{k}_1 \cdot (\mathbf{r} - \mathbf{r}_1)] I_{dc}(\omega_3) I_{db}(\omega_2) I_{ab}(\omega_1), \quad (\text{A10b})$$

$$R_3(-\mathbf{k}_s; \mathbf{k}_3, \mathbf{k}_2, \mathbf{k}_1, \omega_3, \omega_2, \omega_1) = \sum_{abcd} P(a) \int d\mathbf{r} \int d\mathbf{r}_3 \int d\mathbf{r}_2 \int d\mathbf{r}_1 j_{cd}(\mathbf{r}) j_{da}(\mathbf{r}_3) j_{ab}(\mathbf{r}_1) j_{bc}(\mathbf{r}_2) \cdot \exp[-i\mathbf{k}_3 \cdot (\mathbf{r} - \mathbf{r}_3) - i\mathbf{k}_2 \cdot (\mathbf{r} - \mathbf{r}_2) - i\mathbf{k}_1 \cdot (\mathbf{r} - \mathbf{r}_1)] I_{dc}(\omega_3) I_{ac}(\omega_2) I_{ab}(\omega_1), \quad (\text{A10c})$$

$$R_4(-\mathbf{k}_s; \mathbf{k}_3, \mathbf{k}_2, \mathbf{k}_1, \omega_3, \omega_2, \omega_1) = \sum_{abcd} P(a) \int d\mathbf{r} \int d\mathbf{r}_3 \int d\mathbf{r}_2 \int d\mathbf{r}_1 j_{ab}(\mathbf{r}) j_{bc}(\mathbf{r}_3) j_{cd}(\mathbf{r}_2) j_{da}(\mathbf{r}_1) \cdot \exp[-i\mathbf{k}_3 \cdot (\mathbf{r} - \mathbf{r}_3) - i\mathbf{k}_2 \cdot (\mathbf{r} - \mathbf{r}_2) - i\mathbf{k}_1 \cdot (\mathbf{r} - \mathbf{r}_1)] I_{ba}(\omega_3) I_{ca}(\omega_2) I_{da}(\omega_1), \quad (\text{A10d})$$

where  $a, b, c,$  and  $d$  denote the many electron states and  $j_{ab}$  is the matrix element of the current density operator between the states  $a$  and  $b$ .  $I_{ab}(\omega)$  is an auxiliary function representing the Green Function in Liouville space,<sup>8,9</sup>

$$I_{ab}(\omega) = \frac{1}{(\omega - \omega_{ab}) + i\Gamma_{ab}}, \quad (\text{A11})$$

where  $\omega_{ab} = \epsilon_a - \epsilon_b$  is the frequency difference between states  $a$  and  $b$ . Note that  $R_3$  and  $R_4$  are identical to the corresponding quantities in Ref. 7, but  $R_1$  and  $R_2$  are obtained from those of Ref. 7 by changing all  $\mathbf{k}$  to  $-\mathbf{k}$ ,  $\omega$  to  $-\omega$ , and taking a complex conjugate.

**APPENDIX B: LIOUVILLE SPACE PATHWAYS FOR X-RAY FOUR-WAVE MIXING**

In this Appendix we present expressions for x-ray four-wave mixing for the three band core exciton model shown in Fig. 5: The ground, single core-excited-, and double-core-excited states, each state is denoted  $|g\rangle$ ,  $|e\rangle$  (or  $|e'\rangle$ ), and  $|f\rangle$ , respectively. When all incoming x-ray energies are nearly resonant with the single core excitation energies, there are seven Liouville space pathways which survive the RWA, as shown in Fig. 13. Pathways (V)–(VII) include the double-core-excited states, while the (I)–(IV) pathways depend only on the single-core-excited states. We thus obtain the following expressions for each pathway contributing to  $\chi^{(3)}$ .

$$R_I(-\mathbf{k}_3+\mathbf{k}_2-\mathbf{k}_1;\mathbf{k}_3,-\mathbf{k}_2,\mathbf{k}_1,\omega_3-\omega_2+\omega_1,-\omega_2+\omega_1,\omega_1) = \sum_{gee'g'} P(g)J_{g'e';eg}(\mathbf{k}_3-\mathbf{k}_2)J_{g'e';e'g}^*(\mathbf{k}_3-\mathbf{k}_2)I_{eg'}(\omega_3-\omega_2+\omega_1)I_{e'e'}(-\omega_2+\omega_1)I_{eg}(\omega_1), \tag{B1a}$$

$$R_{II}(-\mathbf{k}_3-\mathbf{k}_2+\mathbf{k}_1;\mathbf{k}_3,\mathbf{k}_2,-\mathbf{k}_1,\omega_3+\omega_2-\omega_1,\omega_2-\omega_1,-\omega_1) = \sum_{gee'g'} P(g)J_{g'e';eg}(\mathbf{k}_3-\mathbf{k}_1)J_{g'e';e'g}^*(\mathbf{k}_3-\mathbf{k}_1)I_{eg'}(\omega_3+\omega_2-\omega_1)I_{e'e'}(\omega_2-\omega_1)I_{e'g}(-\omega_1), \tag{B1b}$$

$$R_{III}(-\mathbf{k}_3-\mathbf{k}_2+\mathbf{k}_1;\mathbf{k}_3,\mathbf{k}_2,-\mathbf{k}_1,\omega_3+\omega_2-\omega_1,\omega_2-\omega_1,-\omega_1) = \sum_{gee'g'} P(g)J_{g'e';eg}(\mathbf{k}_2-\mathbf{k}_1)J_{g'e';e'g}^*(\mathbf{k}_2-\mathbf{k}_1)I_{eg'}(\omega_3+\omega_2-\omega_1)I_{g'g}(\omega_2-\omega_1)I_{e'g}(-\omega_1), \tag{B1c}$$

$$R_{IV}(-\mathbf{k}_3+\mathbf{k}_2-\mathbf{k}_1;\mathbf{k}_3,-\mathbf{k}_2,\mathbf{k}_1,\omega_3-\omega_2+\omega_1,-\omega_2+\omega_1,\omega_1) = \sum_{gee'g'} P(g)J_{ge';e'g'}(\mathbf{k}_1-\mathbf{k}_2)J_{ge';eg}^*(\mathbf{k}_1-\mathbf{k}_2)I_{e'g}(\omega_3-\omega_2+\omega_1)I_{g'g}(-\omega_2+\omega_1)I_{eg}(\omega_1), \tag{B1d}$$

$$R_V(-\mathbf{k}_3-\mathbf{k}_2+\mathbf{k}_1;\mathbf{k}_3,\mathbf{k}_2,-\mathbf{k}_1,\omega_3+\omega_2-\omega_1,\omega_2-\omega_1,-\omega_1) = - \sum_{gee'f} P(g)[J_{e'f;fe}(\mathbf{k}_1-\mathbf{k}_2)J_{eg;ge'}(\mathbf{k}_2-\mathbf{k}_1) + J_{fe;ge'}(\mathbf{k}_1-\mathbf{k}_3)J_{fe';ge}^*(\mathbf{k}_1-\mathbf{k}_3)] \cdot I_{fe'}(\omega_3+\omega_2-\omega_1)I_{e'e'}(\omega_2-\omega_1)I_{e'g}(-\omega_1), \tag{B1e}$$

$$R_{VI}(\mathbf{k}_3-\mathbf{k}_2-\mathbf{k}_1;-\mathbf{k}_3,\mathbf{k}_2,\mathbf{k}_1,-\omega_3+\omega_2+\omega_1,\omega_2+\omega_1,\omega_1) = - \sum_{gee'f} P(g)[J_{fe';e'f}(\mathbf{k}_1-\mathbf{k}_3)J_{eg;ge'}(\mathbf{k}_3-\mathbf{k}_1) + J_{eg;e'f}(\mathbf{k}_2-\mathbf{k}_3)J_{fe;ge'}(\mathbf{k}_3-\mathbf{k}_2)] \cdot I_{fe'}(-\omega_3+\omega_2+\omega_1)I_{fg}(\omega_2+\omega_1)I_{eg}(\omega_1), \tag{B1f}$$

$$R_{VII}(-\mathbf{k}_3+\mathbf{k}_2-\mathbf{k}_1;\mathbf{k}_3,-\mathbf{k}_2,\mathbf{k}_1,\omega_3-\omega_2+\omega_1,-\omega_2+\omega_1,\omega_1) = - \sum_{gee'f} P(g)[J_{fe';e'f}(\mathbf{k}_1-\mathbf{k}_2)J_{eg;ge'}(\mathbf{k}_2-\mathbf{k}_1) + J_{fe;ge'}(\mathbf{k}_2-\mathbf{k}_3)J_{eg;e'f}(\mathbf{k}_3-\mathbf{k}_2)] \cdot I_{fe'}(\omega_3-\omega_2+\omega_1)I_{e'e'}(-\omega_2+\omega_1)I_{eg}(\omega_1), \tag{B1g}$$

where  $J_{ab:cd}(\mathbf{k})$  is a tetradic current density matrix element defined as

$$J_{ab:cd}(\mathbf{k}) \equiv \int d\mathbf{r} j_{ab}(\mathbf{r}) j_{cd}(\mathbf{r}) \exp(-i\mathbf{k}\cdot\mathbf{r}). \tag{B2}$$

**APPENDIX C: THE PUMP-PROBE SIGNAL**

The x-ray pump-probe signal is given in Eq. (15). There are two possible permutations of the sequences of two beams in the diagrams (I)–(VII) of Fig. 13, so that altogether 14 pathways contribute to the signal.

Combining Eqs. (A5), (A8), and (15), we obtain

$$W_{PP}(\mathbf{k}_1,\omega_1,\mathbf{k}_2,\omega_2) \propto -\nu_0 \frac{1}{2\hbar^3} \text{Im}[R_I(-\mathbf{k}_2;\mathbf{k}_2,-\mathbf{k}_1,\mathbf{k}_1,\omega_2,0,\omega_1) + R_I(-\mathbf{k}_2;\mathbf{k}_1,-\mathbf{k}_1,\mathbf{k}_2,\omega_2,\omega_2-\omega_1,\omega_2)] \tag{C1a}$$

$$+R_{II}(-\mathbf{k}_2; \mathbf{k}_2, \mathbf{k}_1, -\mathbf{k}_1, \omega_2, 0, -\omega_1) \\ +R_{II}(-\mathbf{k}_2; \mathbf{k}_1, \mathbf{k}_2, -\mathbf{k}_1, \omega_2, \omega_2 - \omega_1, -\omega_1) \quad (C1b)$$

$$+R_{III}(-\mathbf{k}_2; \mathbf{k}_2, \mathbf{k}_1, -\mathbf{k}_1, \omega_2, 0, -\omega_1) \\ +R_{III}(-\mathbf{k}_2; \mathbf{k}_1, \mathbf{k}_2, -\mathbf{k}_1, \omega_2, \omega_2 - \omega_1, -\omega_1) \quad (C1c)$$

$$+R_{IV}(-\mathbf{k}_2; \mathbf{k}_2, -\mathbf{k}_1, \mathbf{k}_1, \omega_2, 0, \omega_1) \\ +R_{IV}(-\mathbf{k}_2; \mathbf{k}_1, -\mathbf{k}_1, \mathbf{k}_2, \omega_2, \omega_2 - \omega_1, \omega_2) \quad (C1d)$$

$$+R_{V}(-\mathbf{k}_2; \mathbf{k}_2, \mathbf{k}_1, -\mathbf{k}_1, \omega_2, 0, -\omega_1) \\ +R_{V}(-\mathbf{k}_2; \mathbf{k}_1, \mathbf{k}_2, -\mathbf{k}_1, \omega_2, \omega_2 - \omega_1, -\omega_1) \quad (C1e)$$

$$+R_{VI}(-\mathbf{k}_2; -\mathbf{k}_1, \mathbf{k}_2, \mathbf{k}_1, \omega_2, \omega_2 + \omega_1, \omega_1) \\ +R_{VI}(-\mathbf{k}_2; -\mathbf{k}_1, \mathbf{k}_1, \mathbf{k}_2, \omega_2, \omega_2 + \omega_1, \omega_2) \quad (C1f)$$

$$+R_{VII}(-\mathbf{k}_2; \mathbf{k}_2, -\mathbf{k}_1, \mathbf{k}_1, \omega_2, 0, \omega_1) \\ +R_{VII}(-\mathbf{k}_2; \mathbf{k}_1, -\mathbf{k}_1, \mathbf{k}_2, -\omega_2, \omega_2 - \omega_1, \omega_1)]. \quad (C1g)$$

It should be noted that while the pump-probe spectrum is given by the imaginary part of  $\chi^{(3)}$ , heterodyne detected four-wave mixing can give both the imaginary and the real parts.

In the long wavelength  $\mathbf{k}=0$  limit,  $W_{PP}$  may be recast in the form,

$$W_{PP}(\mathbf{k}_1, \omega_1, \mathbf{k}_2, \omega_2) = \sum_{i=I}^{VII} \text{Im}[W^i], \quad (C2)$$

where

$$W^I = - \sum_{ee'} J_{ge;eg}(\mathbf{0}) J_{ge';e'g}^*(\mathbf{0}) \{I_{eg}(\omega_2) I_{ee'}(0) I_{eg}(\omega_1) \\ + I_{eg}(\omega_2) I_{ee'}(\omega_2 - \omega_1) I_{eg}(\omega_1)\}, \quad (C3a)$$

$$W^{II} = - \sum_{ee'} J_{ge;eg}(\mathbf{0}) J_{ge';e'g}^*(\mathbf{0}) \{I_{eg}(\omega_2) I_{ee'}(0) I_{ge'}(-\omega_1) \\ + I_{eg}(\omega_2) I_{ee'}(\omega_2 - \omega_1) I_{ge'}(-\omega_1)\}, \quad (C3b)$$

$$W^{III} = - \sum_{ee'} J_{eg;eg}(\mathbf{0}) J_{ge';e'g}^*(\mathbf{0}) \{I_{eg}(\omega_2) I_{gg}(0) I_{ge'}(-\omega_1) \\ + I_{eg}(\omega_2) I_{gg}(\omega_2 - \omega_1) I_{ge'}(-\omega_1)\}, \quad (C3c)$$

$$W^{IV} = \sum_{ee'} J_{ge';e'g}(\mathbf{0}) J_{ge;eg}(\mathbf{0}) \{I_{e'g}(\omega_2) I_{gg}(0) I_{eg}(\omega_1) \\ + I_{e'g}(\omega_2) I_{gg}(\omega_2 - \omega_1) I_{eg}(\omega_2)\}, \quad (C3d)$$

$$W^V = - \sum_{ee'f} (J_{e'f;fe}(\mathbf{0}) J_{eg;ge'}(\mathbf{0}) + J_{fe;ge'}(\mathbf{0}) J_{fe';ge}^*(\mathbf{0})) \\ \times \{I_{fe'}(\omega_2) I_{ee'}(0) I_{ge'}(-\omega_1) \\ + I_{fe'}(\omega_2) I_{ee'}(\omega_2 - \omega_1) I_{ge'}(-\omega_1)\}, \quad (C3e)$$

$$W^{VI} = - \sum_{ee'f} (J_{fe;e'f}(\mathbf{0}) J_{eg;ge'}(\mathbf{0}) + J_{eg;e'f}(\mathbf{0}) J_{fe;ge'}(\mathbf{0})) \\ \times \{I_{fe'}(\omega_2) I_{fg}(\omega_2 + \omega_1) I_{eg}(\omega_1) \\ + I_{fe'}(\omega_2) I_{fg}(\omega_2 + \omega_1) I_{eg}(\omega_1)\}, \quad (C3f)$$

$$W^{VII} = - \sum_{ee'f} (J_{fe;e'f}(\mathbf{0}) J_{eg;ge'}(\mathbf{0}) + J_{fe;ge'}(\mathbf{0}) J_{eg;e'f}^*(\mathbf{0})) \\ \times \{I_{fe'}(\omega_2) I_{ee'}(0) I_{eg}(\omega_1) \\ + I_{fe'}(\omega_2) I_{ee'}(\omega_2 - \omega_1) I_{eg}(\omega_1)\}. \quad (C3g)$$

These equations were used in all calculations represented in this paper.

## APPENDIX D: COULOMB INTERACTIONS

In this appendix we derive Eqs. (8) for on-site Coulomb interactions.

The coefficients of the Coulomb interaction between valence electrons in Eq. (7b) are

$$u_v(\alpha_1 \alpha_2; \alpha_3 \alpha_4) \equiv \int d^3 \mathbf{r} \int d^3 \mathbf{r}' \psi_{\alpha_1}^*(\mathbf{r}) \psi_{\alpha_2}^*(\mathbf{r}') \\ \times \frac{e^2}{|\mathbf{r} - \mathbf{r}'|} \psi_{\alpha_3}(\mathbf{r}') \phi_{\alpha_4}(\mathbf{r}), \quad (D1)$$

where  $\psi_{\alpha}(\mathbf{r})$  is the wave function of the  $\alpha$ th antibonding MO. The wave function  $\psi_{\alpha}(\mathbf{r})$  is represented as a linear combination of AOs with use of  $A_{\alpha m}$  in Eq. (2),

$$\psi_{\alpha}(\mathbf{r}) = \sum_{m=1}^{10} A_{\alpha m} \psi_m(\mathbf{r}), \quad (D2)$$

where  $\psi_m(\mathbf{r})$  is the wave function of the AO at site  $m$ . Substituting Eq. (D2) into Eq. (D1), and assuming on-site Coulomb interaction, we obtain Eq. (8a), where  $u_v$  is defined by

$$u_v \equiv \int d^3 \mathbf{r} \int d^3 \mathbf{r}' \psi_m^*(\mathbf{r}) \psi_m^*(\mathbf{r}') \frac{e^2}{|\mathbf{r} - \mathbf{r}'|} \psi_m(\mathbf{r}') \phi_m(\mathbf{r}). \quad (D3)$$

For simplicity, we assume an identical value of  $u_v$  for all sites.

The coefficients  $u_{lv}(\alpha_1, \alpha_2)$  in Eq. (7d) are obtained in the same way. The Coulomb interaction coefficients between a core hole at site  $l$  and a valence electron in Eq. (7d) is

$$u_{lv}(\alpha_1; \alpha_2) \equiv \int d^3 \mathbf{r} \int d^3 \mathbf{r}' \phi_l^*(\mathbf{r}) \psi_{\alpha_1}^*(\mathbf{r}') \\ \times \frac{e^2}{|\mathbf{r} - \mathbf{r}'|} \psi_{\alpha_2}(\mathbf{r}') \phi_l(\mathbf{r}), \quad (D4)$$

where  $\phi_l(\mathbf{r})$  is the N 1s wave function for the core orbital at the site  $l$ . Substituting Eq. (D2) into Eq. (D4) and assuming on-site Coulomb interaction, we finally obtain Eq. (8b), where  $u_l$  is defined by

$$u_l \equiv \int d^3 \mathbf{r} \int d^3 \mathbf{r}' \phi_l^*(\mathbf{r}) \psi_l^*(\mathbf{r}') \frac{e^2}{|\mathbf{r} - \mathbf{r}'|} \psi_l(\mathbf{r}') \phi_l(\mathbf{r}). \quad (D5)$$

- <sup>1</sup> *Proceedings of the Eleventh International Conference on X-ray Absorption Fine Structure XAFS XI*, J. Synchrotron Radiat. **8**, Part 2 (2001).
- <sup>2</sup> J. J. Rehr and R. C. Albers, *Rev. Mod. Phys.* **72**, 621 (2000).
- <sup>3</sup> *Proceedings of VUV-XIII*, July 2001, Trieste, Italy.
- <sup>4</sup> A. Kotani and S. Shin, *Rev. Mod. Phys.* **73**, 203 (2001), and references therein.
- <sup>5</sup> J. Nordgren and E. Z. Kurmaev, *J. Electron Spectrosc. Relat. Phenom.* **110-111**, 1 (2000).
- <sup>6</sup> F. Gel'mukhanov and H. Ågren, *Phys. Rep.* **312**, 87 (1999).
- <sup>7</sup> S. Tanaka, V. Chernyak, and S. Mukamel, *Phys. Rev. A* **63**, 063405 (2001).
- <sup>8</sup> S. Tanaka and S. Mukamel, *Phys. Rev. A* **64**, 032503 (2001).
- <sup>9</sup> S. Mukamel, *Principles of Nonlinear Spectroscopies* (Oxford University Press, New York, 1995).
- <sup>10</sup> A. H. Chin, R. W. Sconenlein, T. E. Glover, P. Baling, W. P. Leemans, and C. V. Shank, *Phys. Rev. Lett.* **83**, 336 (1999).
- <sup>11</sup> P. M. Rentzepis and J. Helliwell, *Time-Resolved Electron and X-Ray Diffraction* (Oxford University Press, New York, 1995).
- <sup>12</sup> V. Srajer, T. Y. Teng, T. Ursby, C. Prodervand, Z. Ren, S. Adachi, W. Schildkamp, D. Bourgeois, M. Wulff, and K. Moffat, *Science* **274**, 1726 (1996).
- <sup>13</sup> C. W. Siders, A. Cavalleri, K. Sokolowski-Tinten, C. S. Toth, T. Guo, M. Kammler, M. Horn von Hoegen, K. R. Wilson, D. van der Linde, and C. P. J. Barty, *Science* **286**, 1340 (1999).
- <sup>14</sup> C. R. Petrucci, R. Jimenez, T. Guo, A. Cavalleri, C. W. Siders, F. Raski, J. A. Squier, B. C. Walker, K. R. Wilson, and C. P. J. Barty, *Nature (London)* **398**, 310 (1999).
- <sup>15</sup> I. V. Tomov, D. A. Oulianov, P. Chen, and P. M. Rentzepis, *J. Phys. Chem. B* **103**, 7081 (1999).
- <sup>16</sup> L. X. Chen, W. J. H. Jäger, G. Jennings, D. J. Gosztola, A. Munkholm, and J. P. Hessler, *Science* **292**, 262 (2001).
- <sup>17</sup> M. Drescher, M. Hentschel, R. Kienberger, G. Tempea, C. Spielmann, G. A. Reider, P. B. Corkum, and F. Krausz, *Science* **291**, 1923 (2001); M. Hentschel *et al.*, *Nature (London)* **414**, 509 (2001).
- <sup>18</sup> K. Siegbahn, C. Nordling, A. Fahlman, R. Nordberg, K. Hamrin, J. Hedman, G. Johansson, T. Bergmark, S. -E. Karlsson, I. Lindgren, and B. Lindberg, *ESCA-Atomic, Molecular and Solid State Structure Studied by Means of Electron Spectroscopy*, Nova Acta Regiae Soc. Sci. Upsaliensis, Series IV (Almqvist and Wiksell, Uppsala, 1967).
- <sup>19</sup> H. Ågren, B. O. Roos, P. S. Bagus, U. Gelius, P.-Å. Malmquist, S. Svensson, R. Maripuu, and K. Siegbahn, *J. Chem. Phys.* **77**, 3893 (1982).
- <sup>20</sup> A. R. Slaughter, M. S. Banna, and C. A. McDowell, *Chem. Phys. Lett.* **98**, 531 (1983).
- <sup>21</sup> H.-J. Freund, A. R. Slaughter, S. M. Ballina, M. S. Banna, R. W. Bigelow, B. Dick, J. Lex, and H. M. Deger, *J. Chem. Phys.* **81**, 2535 (1984).
- <sup>22</sup> C. C. Turci, S. G. Urquhart, and A. P. Hitchcock, *Can. J. Chem.* **74**, 851 (1996).
- <sup>23</sup> J. Stöhr, *NEXAFS Spectroscopy* (Springer-Verlag, Berlin, 1991).
- <sup>24</sup> O. Plashkevych, L. Yang, O. Vahtras, H. Ågren, and L. G. M. Pettersson, *Chem. Phys.* **222**, 125 (1997).
- <sup>25</sup> J. B. Foresman and A. Frisch, *Exploring Chemistry with Electronic Structure Methods* (Gaussian, Inc., Pittsburgh, PA, 1996).
- <sup>26</sup> P. M. Platzman and E. D. Isaacs, *Phys. Rev. B* **57**, 11107 (1998).
- <sup>27</sup> P. Abbamonte, C. A. Burns, E. D. Isaacs, P. M. Platzman, L. L. Miller, S. W. Cheong, and M. V. Klein, *Phys. Rev. Lett.* **83**, 860 (1999).
- <sup>28</sup> H. Enkisch, A. Kaprolat, W. Schülke, M. H. Krisch, and M. Lorenzen, *J. Phys. Chem. Solids* **61**, 449 (2000).
- <sup>29</sup> Y. Ma, K. E. Miyano, P. L. Cowan, Y. Aglitzkiy, and B. A. Karlin, *Phys. Rev. Lett.* **74**, 478 (1995).
- <sup>30</sup> H. Haug and S. W. Koch, *Quantum Theory of the Optical Electronic Properties of Semiconductors*, 3rd ed. (World Scientific, Singapore, 1994).
- <sup>31</sup> V. Chernyak, W. M. Zhang, and S. Mukamel, *J. Chem. Phys.* **109**, 9587 (1998).
- <sup>32</sup> O. Gunnarsson and K. Schonhammer, *Phys. Rev. B* **28**, 4315 (1983).
- <sup>33</sup> *Core-Level Spectroscopy in Condensed Systems*, edited by J. Kanamori and A. Kotani (Springer-Verlag, New York, 1988).
- <sup>34</sup> The definition of the dephasing time is different from that defined in the theoretical analysis on resonant x-ray emission where the dephasing rate is defined as the inverse time of the detuning energy from resonance (Ref. 6). Although this definition is useful as a figure of merit for coherence of second-order coherent process, in this paper, in order to keep consistency in terminologies with optical nonlinear spectroscopy (Ref. 9), we defined Eq. (18) as the dephasing rate as commonly used in analyses of optical nonlinear spectroscopies.
- <sup>35</sup> E. J. McGuire, *Phys. Rev.* **185**, 1 (1969).
- <sup>36</sup> E. Pahl, J. Brand, L. S. Cederbaum, and F. Tarantelli, *Phys. Rev. A* **60**, 1079 (1999).
- <sup>37</sup> T. Privalov, F. Gel'mukhanov, and H. Ågren, *Phys. Rev. B* **59**, 9243 (1999).
- <sup>38</sup> S. Tanaka and Y. Kayanuma, *Solid State Commun.* **64**, 77 (1996).
- <sup>39</sup> S. Tanaka, K. Ueda, and Y. Kayanuma, *Phys. Rev. A* **57**, 3437 (1998).
- <sup>40</sup> A. Tortschanoff, A. Piryatinski, and S. Mukamel, *J. Lumin.* (in press).
- <sup>41</sup> S. Tomimoto, H. Nansei, S. Saito, T. Suemoto, J. Takeda, and S. Kurita, *Phys. Rev. Lett.* **81**, 417 (1998).
- <sup>42</sup> S. L. Dexheimer, A. D. Van Pelt, J. A. Brozik, and B. I. Swanson, *Phys. Rev. Lett.* **84**, 4425 (2000).
- <sup>43</sup> B. I. Swanson, J. A. Brozik, S. P. Love, G. F. Strouse, A. P. Shreve, A. R. Bishop, and W.-Z. Wang, *Phys. Rev. Lett.* **82**, 3288 (1999).